RSC Advances

ROYAL SOCIETY OF CHEMISTRY

www.rsc.org/advances

Supercritical Synthesis of Magnetite-Reduced Graphene Oxide Hybrid with Enhanced Adsorption Properties toward Cobalt & Strontium Ions

Ahmad Tayyebi*, Mohammad Outokesh*

Department of Energy Engineering, Sharif University of Technology, Azadi Ave. P.O. Box: 113658639, Tehran, Iran.

*Corresponding author's email address: Outokesh@sharif.edu, atayebi162@gmail.com

Abstract

The current study presents a supercritical synthesis of magnetite-reduced graphene oxide (M-RGO)in methanol medium, in which Fe_3O_4 nanoparticles are simultaneously formed, surface modified and decorated on the surface of the reduced graphene oxide. Simulation by density functional theory which was performed using M06-2x/cc-pVDZ level of theory indicates that upon adsorption of Fe_3O_4 cluster on the graphene, the overall charge on the graphene surface becomes about 0.0236e negative, indicating charge transfer from Fe_3O_4 cluster to the graphene surface. Instrumental and chemical analyses exhibited formation of strong bonds between Fe_3O_4 and graphene, through C-O-Fe and C-Fe bridges. Based on this data the study puts forward a formation mechanism for M-RGO. The adsorption behaviors of the M-RGO towards Co^{2+} and Sr^{2+} ions represented appreciably higher uptake capacity than magnetite- graphene oxide (M-GO), a zero zeta potential point at pHs≈2, endothermic and spontaneous adsorption, and a fast kinetics that was controlled by chemical reaction between ions and surface active sites of Fe_3O_4 nanoparticles. The material also showed, a good reusability, a quick elution by 0.5 $mol.dm^{-3}$ HCl, and most importantly, simple separation from the solution by a magnet. Overall, the M-RGO appears to be a promising alternative for current magnetite-graphene oxide hybrids in adsorption of heavy metal ions.

Keywords: Supercritical methanol, Magnetite-Reduced graphene oxide, Surface modification, Formation mechanism, Adsorption

Introduction: In recent decades, water pollution has been one of the most important millstones around every society's neck due to the shortage of clean water resources. This pollution which is arisen from deliberate disposal of organic-inorganic effluents (e.g. toxic metal ions) into fresh water has resulted in a worldwide environmental concern, and serious health problems.[1]

As for treatment of the contaminated water, so far, various methods have been developed including among the others: chemical precipitation, membrane technology, photocatalytic process and adsorption.[2]

Adsorption is a fast, inexpensive, and universal method for treatment and purification of water. Consequently, so far, a great deal of adsorbents have been tested, and commercially exploited in water treatment processes, namely activated carbon, inorganic adsorbents (e.g. zeolites), and ion exchange resins.[3] Despite such efforts, development of new, efficient and low-cost adsorbents is still favored by the water treatment industries. In particular, demand for an available, and low cost adsorbent of heavy metal ions, that encompasses both a large surface area, and a simple functionalization process is quite high.

When one seeks huge surface area, and abundant functional groups, graphene oxide (GO) arises as one of the best candidate. Graphene oxide is a single sheet of carbon atoms which hosts a great deal of oxygen functionalities such as epoxy (-O-) and hydroxyl (-OH) in its inner area,[4] and carboxylic groups in its edges.[5] Presence of these functionalities makes the surface of GO an ideal template for nucleation and growth of useful nanoparticles (NPs) such as Au,[6] Ag,[7] Pt,[8] TiO_2,[9] and Fe_3O_4.[10] Among these graphene-based nanomaterials, magnetite-graphene hybrid has been recognized as a promising material for various applications including lithium-ion batteries,[11] drug delivery,[12] sensor fabrication,[13] MRI contrast enhancement,[10] photothermal therapy,[14] protective surface coatings,[15] and adsorbent synthesis.[16]

As for synthesis of magnetite–graphene hybrid, so far a number of methods have been devised including coprecipitation[10], solvothermal[17], hydrothermal,[14] and sonochemical techniques[16]. However, obstacles in preparation of magnetite nanoparticles such as necessity for accurate pH adjustment, preparing inert atmosphere, controlling the Fe(II):Fe(III) molar ratio, and exploiting the toxic organic solvents and reducants[18] has given rise to need for an alternative method to circumvent all these hurdles. This new method, should additionally support surface modification of the magnetite NPs, which is a vital stage in improving their adsorption properties.

In recent decades, supercritical fluids have attracted much attention as synthesis media owing to their exclusive properties including low viscosity, high diffusivity, negligible surface tension, and environmental benignity[19,20]. Such properties are particularly useful for synthesis of nanoparticles or more in general, nanomaterials.[21] Amongst the oxides of iron, hematite (α-Fe_2O_3) was fabricated in supercritical water,[22] while magnetite NPs were reportedly prepared in the supercritical alcohols e.g. methanol or ethanol[19]. The reducing effect of supercritical alcohols is primarily attributed to the dissociated hydroxide ions (OH^-),[23] that are formed at supercritical condition. These hydroxide ions, not only cause formation of the metal[24, 25] or metal oxides with low oxidation states (e.g. Fe_3O_4, ZnO)[19, 26], but also are able to reduce graphene oxide nanosheets.[27]

When extensive investigation demonstrated that deposition of some NPs on GO brings about enhanced physiochemical properties compared to the pure graphene or pristine NPs (i.e. synergism),[28-30] a lot of interest was devoted to fabrication of the GO-NPs hybrid and elucidation of their properties. Shao et al. showed that intercalation of NPs between the graphene sheets attenuates the π-π interaction, and in turn prevents stacking of the graphene layers (i.e. restoring

of the graphite structure).[31] Other researchers emphasized on the role of metal-O-C connection in grafting of the metal oxide NPs on the surface of graphene.[32, 33] Song and co-workers demonstrated that flower like ZnO is connected to the surface of GO through Zn-O-C bonds.[32] According to Nethravathi et al. negative oxygen functionalities on the surface of GO sequester the positive Pt^{4+} ions through the C-O-Pt chemical bond, formed by consecutive transient-complex formation and dehydration steps.[8] Despite such great efforts, most of the accomplished researches dealt with connection mechanism onto the GO rather than the reduced GO (RGO). Indeed, in the case of supercritical alcohols, in which NPs are connected to the RGO, lesser information is available.

The current study is aimed at elaboration of the following issues:

- Supercritical synthesis of magnetite-reduced graphene oxide (M-RGO) in methanol.
- Finding plausible mechanisms for surface modification of magnetite NPs and connection of them onto the graphene surface.
- Elucidation of the adsorption properties of M-RGO for Sr^{2+} and Co^{2+} ions, and its comparison with those of magnetite NPs and RGO.

The ultimate goal of this work is to synthesize a new graphene-based adsorbent with the potential environmental applications.

Experimental Section

Material and Methods: Natural high purity flake graphite, sulfuric acid 98%, hydrochloric acid 37%, hydrogen peroxide 30%, iron (III) nitrate hexahydrate, methanol, sodium nitrate, and potassium permanganate, were all purchased from Merck AG (Darmstadt, Germany) and used without purification.

Synthesis of graphene oxide (GO): Graphene Oxide (GO) was synthesized from high purity graphite using the modified Hummers- Hoffman's method.[34] In a typical procedure, a mixture of 2 g graphite powder and 2 g sodium nitrate was dispersed in 45 cm^3 of 98% (w/w) sulfuric acid. While the temperature was maintained below 5 ^oC using an ice bath, 6 g potassium permanganate was gradually added to the dispersion within a period of 2 h. Then, the mixture was stirred for 30 min, after that, 100 cm^3 distillated water was slowly added to it. At this stage, temperature was increased to 95 ^oC, and the mixture was kept at such temperature for 30 min. Afterward, the hot slurry was cooled to 40 ^oC by adding 300 cm^3 distillated water, and the reaction was terminated using 20 cm^3 of a 30% (w/v) hydrogen peroxide solution. The obtained mixture was filtered, washed with dilute (5% w/v) HCl solution to remove metal ions, and repeatedly washed (with distilled water) and centrifuged until the pH becomes 5. Finally the produced GO was dried at ambient temperature.

Synthesis of Magnetite-Reduced Graphene Oxide (M-RGO): About 0.1 g graphene oxide (GO) was dispersed in 100 cm^3 methanol (1mg/ml) and the dispersion was sonicated by an ultrasonic bath (Elmasonic, S 30H ,Branson, CT, USA) until the solution became clear. Next, 10 cm^3 of a 2.5 mol/l of iron nitrate (III) solution was added to the foregoing solution. Then, 15 cm^3 of the obtained mixture was poured into a 30 cm^3 stainless steel autoclave, and the autoclave was inserted in a furnace to effect the M-RGO synthesis at supercritical condition. The employed autoclave was able to endure working temperature and pressure of 500 °C and 550 atm, respectively; but in order to keep adequate safety margin, it was always loaded with 50% of its capacity (Figure S1 in supporting information).

Due to the small size of the reactor, and the intensive rate of heating, the warm up time for surpassing the critical point was quite short and less than10 min. Residence time which is

defined as "heating period at the temperature set point", was about 15 min. The reaction vessel after removing from the furnace was rapidly quenched by cold water and the obtained material was separated from the solution by a magnet. The M-RGO hybrid prepared by this method was transferred to some Petri dishes and dried in nitrogen atmosphere. Figure S1 in Supporting Information presents a schematic illustration of the M-RGO fabrication process. In addition to the M-RGO, we also prepared the reduced graphene oxide (RGO) by charging of the GO-methanol solution into the autoclave, and its treatment exactly with the same manner as M-RGO.

Adsorption tests: All of the adsorption tests were batchwise. In every test, about 20 mg of adsorbent was charged into a conical flask, which contained 20 cm^3 of Co^{2+} or Sr^{2+} solutions. Next, the mixture was ultrasonicated for a certain period, after which, the M-RGO particles were separated from the solution by a magnet placed behind the vessel wall. Finally, concentration of the decanted supernatant was measured by atomic adsorption spectrometry (AAnalyst, 800, PerkinElmer, USA).

In order to investigate the effect of pH on the uptake, pH of the Co^{2+} or Sr^{2+} solutions was adjusted on the desired values between 1 to 10, by accurate addition of the HCl or NaOH solutions. Kinetics of the adsorption, and uptake capacity of the M-RGO were studied by conducting the above-mentioned batch experiments in different time intervals, and target-ion concentrations. All of the experiments were conducted at pH 6.5, except the ones that investigated the effect of pH. Moreover, the initial concentrations of Sr^{2+} and Co^{2+} in all of the experiments were 50 ppm except the ones related to the adsorption isotherms

In analysis of the adsorption data, adsorption capacity (Q), uptake percentage (R, %), fractional attainment to equilibrium (X), and distribution coefficient (K_d) were defined as:

$$Q = \frac{(C_0 - C_e)V}{m} \quad (1)$$

$$R, \% = \frac{C_0 - C_e}{C_0} \times 100 \quad (2)$$

$$X = \frac{C_0 - C_t}{C_0 - C_e} \quad (3)$$

$$K_d = \frac{C_0 - C_e}{C_e} \times \frac{V}{m} \quad (4)$$

where C_0, C_t, and Ce(ppm), denote concentrations of the solution at initial, time "t", and equilibrium, respectively; m (g) is mass of the adsorbent, and V(cm^3), volume of the solution.

In order to elucidate the adsorption properties of M-RGO in a more detailed fashion, we compared them with those of magnetite NPs and magnetite-graphene oxide hybrid (M-GO) on adsorption of Co^{2+} and Sr^{2+} ions. The required M-GO for this purpose was synthesized by the ultrasound assisted co-precipitation method, which has been described elsewhere.[16]

Characterization: Morphological microscopic pictures of the GO nanosheets and M-RGO hybrid were obtained using low and high-resolution transmission electron microscopy (TEM / HRTEM, JEOL, JEM-2100, Japan). The employed HRTEM mode also supported the selected area electron diffraction (SAED) and energy dispersive X-ray (EDX) analysis of the samples. Atomic force microscopy (AFM, Park Scientific CP-Research model, VEECO) was used to find the thickness and morphology of the GO and M-RGO hybrid. The employed AFM system worked in the tapping mode, with frequency of 320 kHz, and by using a 20 nm thick silicone tip.

Samples for AFM imaging were prepared by drop casting of dilute GO and M-RGO suspensions onto a clean mica substrate.

Raman spectroscopy (SENTERRA BRUKER, Germany) was performed on the samples at room temperature using a 785 nm Nd-YAG laser excitation source to scrutinize changing of the chemical and crystalline structure during the synthesis process. Meanwhile, the X-ray photoelectron spectroscopy (XPS) revealed the chemical states of the GO and M-RGO nanosheets. The XPS instrument was equipped with a hemispherical analyzer, a data acquisition system, and an Al-K_α X-ray source (hv=1486.6 eV) operating at pressure lower than 10^{-7} Pa. The XPS peaks were deconvoluted by Gaussian components model after Shirley background subtraction. The X- ray diffractometry (Rigaku Miniflex XRD, Texas, U.S.A.) and Fourier transforms infrared spectroscopy (FTIR, Perkin-Elmer, SpectrumRX, USA) were respectively used for crystallographic and chemical bond analysis of the prepared materials.

The magnetic hysteresis cycle of the powdered M-RGO was obtained by a QMPS SQUID magnometer at the field range of -1T to 1T at room temperature. Optical characteristics of the diluted GO and M-RGO suspensions (0.01 mg/cm^3) were studied by a UV-Visible spectrophotometer (PerkinElmer UV-Vis-NIR model Lambda 950, USA).

A “Malvern Zetasizer nano ZS” instrument was used to measure the zeta potentials of all prepared samples at 25°C. Samples prepared for the dynamic light scattering (DLS) measurements were loaded into a pre-rinsed folded capillary cell for the zeta potential measurements.

In order to study the thermal stability and composition of the prepared materials, thermo-gravimetric analysis (TGA) was performed in air atmosphere using a simultaneous thermal

analyser (TGA/DSC 1, METTLER TOLEDO, Switzerland). A heating rate of 10 ^{o}C /min was utilized in those experiments.

Density Functional Theory Calculations: To better understand the nature of interaction between graphene and (Fe_3O_4) cluster, we undertook a density functional calculation using circumcoronene ($C_{54}H_{18}$) composed of 19 aromatic rings as a model of graphene.[35] In our model, all the boundary carbon atoms of the circumcoronene have been saturated with hydrogen atoms (see Figure 8) and thus, the (Fe_3O_4) cluster just interacts and sequestered on the carbon atoms of the circumcoronene. Full optimization and property calculations for the adsorption of (Fe_3O_4) cluster on the graphene surface (circumcoronene model) were done at M06-2X[36] method using Dunning cc-pVDZ basis set by Gaussian 03 program.[37] All of the calculations were carried out without symmetry restrictions. The harmonic vibrational frequencies and the corresponding zero-point vibrational energies (ZPVEs) were calculated for all of the optimized geometries, and real frequencies were obtained in all cases.

Results and discussions

Figure 1a exhibits an AFM image of the prepared GO, in which the thickness of the sheet corresponds to the height of the white-marked line, depicted in Figure 1a. The height profile shows two monolayer GO sheets with the thickness of around 0.8 nm. Due to the presence of oxygen containing groups on both sides of GO surface, it is broadly accepted that thickness of a single GO layer is around 0.9 nm which is 0.5 nm thicker than a 0.4 nm typical graphene sheet.[38]

According to Figure 1b, the UV-vis absorption peak of the GO suspension appears at 227 nm, while for the reduced graphene oxide (RGO), it emerges at 253 nm, indicating a red-shift arisen from the electronic conjugation of the graphene sheets, restored upon the reduction. For

M-RGO the absorption peak appears at 244 nm as a result of intercalation of magnetite nanoparticles between graphene sheets that results in attenuation of the restoring process.

[Insert Figure 1 about Here]

Figure S2a in supporting information shows XRD patterns of synthesized materials in which characteristic peak of graphite emerges at 2θ=26 (Interlayer space, d~0.4nm). As a result of intercalation of oxygen functionalities and water, the position of XRD peak of GO shifted to lower degree (2θ=11) corresponding to larger interlayer space (d~0.8 nm). The XRD patterns of the reduced graphene oxide (RGO) presents a broad and low intensity peak at 2θ=24 indicating amorphous nature of the RGO (Figure S2a), obtained at high temperature and pressure conditions of supercritical ethanol.

The XRD pattern of M-RGO hybrid depicts seven characteristic peaks at 30.1°, 35.4°, 37.1°, 43.1°, 53.4°, 56.9° and 62.5°, that are respectively corresponding to (220), (311), (222), (400), (422), (511) and (440) planes of the magnetite (Fe_3O_4) crystal. No peak of hematite (α-Fe_2O_3) or other impurities is detected in the XRD pattern of the M-RGO. In addition, presence of a broad and low intensity peak around $2\theta=24^0$ indicates incorporation of graphene sheet in the M-RGO structure, whose extent is lesser than the RGO alone.

Figure S2b in supporting information represents Raman spectra of the as-prepared materials with a D-band at 1350 cm^{-1} and a G-band at 1580 cm^{-1}. In M-RGO sample, 5 characteristic peaks including $A_{1g}(1)+E_g(1)$, $E_g(2)+E_g(3)$, $E_g(4)$, $A_{1g}(2)$ and $E_g(5)$ define finger print of Fe_3O_4 NPs at 223.5 cm^{-1}, 289 cm^{-1}, 404 cm^{-1}, 491 cm^{-1} and 604.5 cm^{-1}, respectively.

Morphology and crystalline structures. It seems to be worthwhile to study the effect of supercritical methanol on morphology and structure of GO, RGO, and M-RGO. In this regards,

low magnification TEM images and SAED patterns of the prepared materials are illustrated in Figure 2. The wrinkled sheets of GO is depicted in Figure 2a, in which the transparent region indicated by the arrow most likely corresponds to monolayer graphene sheets. The SAED pattern of GO in inset Figure 2a shows the diffraction spots and resolved ring along the [001] zone axis of GO confirming the hexagonal crystal structure of the GO. According to Figure 2b, increasing of temperature over 350 ^{o}C and reaching the supercritical conditions leads to disappearance of diffraction spots and resolved rings in the SAED pattern of GO, as a result of formation of the reduced graphene (RGO) with a mild crystalline structure. This is in a good agreement with the XRD results (Figure S2a) in which RGO exhibits a broad and low intensity peak, corresponding to the amorphous structure. In the case of M-RGO hybrid, grafting of Fe_3O_4 nanoparticles (NPs) on the graphene surface (Figure 2c), resulted in random distribution of diffraction spots between the SAED rings.

[Insert Figure 2 about Here]

Figure 3 presents more accurate SEM and TEM images of the Fe_3O_4 NPs that were decorated on the GO surface, using supercritical methanol. Oxygen functionalities on the GO surface act as active sites for nucleation and growth of Fe_3O_4 NPs. In addition, large number of oxygen-containing groups means more available space for deposition of the Fe_3O_4 NPs, and thus lower agglomeration of the magnetite particles. Figure 3a demonstrates SEM image of Fe_3O_4 NPs on the surface of graphene sheets. Figure 3b displays a TEM image of M-RGO, according to which, average size of the magnetite nanoparticles was found about 15 nm (Figure S3). Elemental analysis of GO, RGO, and M-RGO was further evidenced by energy dispersive X-ray analysis (EDX) (Figure S4 in supplementary information), that demonstrated absence of any

elemental impurity other than Fe, C, and O in the M-RGO hybrid, as well as the reduction effect of supercritical methanol on GO.

Figure 3c demonstrates HRTEM image of the Fe_3O_4 NPs whose 0.2 nm inter-planar spacing corresponds to the distance between two (222) plans of the magnetite.

[Insert Figure 3 about Here]

Aggregation of carbon-based nanomaterials such as graphene reduces the surface area of their particles in the aquatic system, and results in the reduced adsorption ability. In this respect, we characterized aqueous dispersion of GO, M-RGO, and RGO using dynamic light- scattering (DLS). As it can be seen in Figure 4, the nominal effective diameters which were estimated by the spherical particle model for GO, M-RGO, and RGO were about 750, 850, and 1150 nm, respectively. Due to the aggregation of GO sheets during their reduction in supercritical methanol (SCMeOH), the average diameter of RGO was 1.5 times larger than GO. Deposition of magnetite nanoparticles between graphene layers lowered the aggregation rate of M-RGO, and consequently reduced their average sizes.

[Insert Figure 4 about Here]

Magnetic properties: Figure 5 shows magnetization hysteresis curves of the magnetite NPs, and M-RGO hybrid, synthesized in SCMeOH (inset photograph shows M-RGO dispersed in aqueous solution (left) and that in the presence of a magnet (right)). As it can be seen in the upper inset Figure 5, the saturation magnetization ($\mathbf{M}_S$), and remanence ($\mathbf{M}_R$) for M-RGO are 60 and 12.5 $emu.g^{-1}$, respectively. In comparison with the pure Fe_3O_4 NPs, M-RGO hybrid demonstrates lower magnetic intensities due to the presence of the graphene, as a diamagnetic material that can reduce the superparamagnetic property of the Fe_3O_4.

Another phenomenon that may stand as a reason for lowering of the magnetic property of the M-RGO compared to pure magnetite, is the smaller size of Fe_3O_4 NPs that are formed on the surface of the M-RGO. As was reported by Mahmudi et al. magnetic saturation decreases with decreasing of the size of Fe_3O_4 NPs appreciably.[39] It was demonstrated in the morphology section, that presence of enormous surface area and oxygen functionalities on the surface of GO causes formation of Fe_3O_4 NPs of very small size in M-RGO hybrid. In order to have a quantitative evaluation of the size effect, we measured the size distribution of Fe_3O_4 NPs in both pure magnetite nanoparticles and M-RGO, and compared them with each other. Diffraction light scattering (DLS) analysis of the pure Fe_3O_4 NPs in water (Figure S5 in supporting information) represents an average size of 25 nm. The TEM image of M-RGO (Figure S3 in supporting information) when analyzed by Microstructure Measurement Software resulted in the histogram of Fe_3O_4 NPs on the surface of graphene sheets from which the average size of Fe_3O_4 NPs was obtained 15 nm. Besides the above direct methods, there is another indirect method for measurement of the size of the Fe_3O_4 NPs. This second method is based on the famous Langevin's equation, which correlates average size of the Fe_3O_4 NPs to their saturated magnetization and magnetic susceptibility as follows:

$$D_{Fe_3O_4} = \left(\frac{18 k_B T}{\pi \mu_0 \rho_{Fe_3O_4} {M_S}^2} \left(\frac{dM}{dH} \right)_{H \to 0} \right)^{1/3} \quad (5)$$

$$D_{M-GO} = \left(\frac{18 k_B T}{\pi \mu_0 \rho_{Fe_3O_4} {M^*_S}^2} \left(\frac{dM}{dH} \right)_{H \to 0} \right)^{1/3} \quad (6)$$

where k_B denotes Boltzmann's constant (1.38×10^{-23} J/K), μ_0 shows the permeability of free space ($4\pi \times 10^{-7}$ N/A^2), $\rho_{Fe_3O_4}$ (kg/m^3) indicates density of the magnetite (5180 kg/m^3), M_S stands for the

saturated magnetization, $\left(\frac{dM}{dH}\right)_{H\to 0}$ is susceptibility of the M-RGO at zero field obtained from magnetization curve (Figure 5), and eventually T =298 K is the measurement temperature. For the M-RGO composites, effective saturated magnetization (M_S^*, eq (7)) was obtained from measurement of the Fe_3O_4 content of its samples by wet chemical method (M_s^*=mass percentage of Fe_3O_4 in M-RGO hybrid). The wet chemical analysis was performed by dissolving of about 0.01 g of M-RGO hybrid in 20 cm^3 of concentrated hydrochloric acid, and measurement of its iron content by atomic absorption spectrometry (AAS).[16]

Table (1) indicates the results of estimation of the size of Fe_3O_4 NPs in pure magnetite and in M-RGO by both direct and Langevien methods. Evidently, there is a fair consistency between the two methods. The accuracy of the modified Langevien equation in evaluation of the size of Fe_3O_4 NPs in magnetite-graphene hybrid, and application of the wet chemical method in its implementation was previously reported elsewhere.[16]

[Insert Figure 5 about Here]

[Insert Table 1 about Here]

Chemical composition: The XPS analysis was performed to find out the compositions of the GO, RGO, and M-RGO samples. In order to study the XPS results, the binding energies were standardized using carbon peak at 284.8 eV as a reference peak, and the relative intensity of other peaks were estimated from the area under the curves by integrating the peak areas.[40] The full scan survey of GO and RGO in Figure 6a represents only two peaks at 285 and 532 eV (which are assigned to C(1s) and O(1s) core levels).[41] The intensity of O1(s) core level peak of RGO decreased notably relative to GO, as a result of deoxygenation of the GO in the supercritical methanol. Full scan survey of M-RGO indicates the presence of Fe3p and Fe2p core

level peaks that confirms formation of Fe_3O_4 NPs (Figure 6a). The XPS peaks corresponding to Fe2p core level of Fe_3O_4 NPs is shown in Figure S6 in which Fe2p energy level of iron atoms is divided into two distinct levels of $Fe2p_{3/2}$ at 711.8 eV and $Fe2p_{1/2}$ at 724.4 eV. It should be noted that the energy splitting width is around 12.6 eV that corresponds to a spin-orbit coupling effect, and it is within the standard reference value of Fe_3O_4 NPs.

Figure 6b, c, and d show the C1s core level peak deconvolution of GO, RGO, and M-RGO, respectively. Noticeable presences of oxygen functionalities in the structure of GO was indicated in Figure 6b. The oxygen-containing functional groups were attenuated on the surface of RGO, compared to GO, as a result of reducing effect of SCMeOH (Figure 6b).

As it can be seen in Figure 6b and c, there are two significant differences between C1s core levels of M-RGO and GO as: First, increasing of the C/O ratio in the M-RGO through reduction of GO, and second, emerge of Fe-C, Fe-O-C, and pi-pi peaks in M-RGO hybrid, which indicates formation of Fe_3O_4 NPs, and their connection to the surface of graphene via chemical bonding (Figure 6d).

[Insert Figure 6 about Here]

The O1s core level peak also provides valuable information about the nature of chemical bonds on the surface of M-RGO hybrid. As it can be seen in the Figure S7 in supporting information, the O1s peak in M-RGO hybrid is broader than that of the GO. This phenomenon is presumably attributed to the change in the number of chemical bonds of oxygen atoms. Indeed, due to some sort of chemical interaction (bonding) between iron or oxygen atoms with RGO surface, (See "Density Functional Theory" section), the full width at half maximum (FWHM) of O1s in M-RGO (6 eV) increases compared to GO (4.1 eV). To prove the presence of new chemical bonds in M-RGO composites, O1s spectra of GO and M-RGO were deconvoluted and

shown in Figure 7a, and b. In Figure 7a, the O1s peak of GO includes two spectral peak at 532.2 and 533.3 eV, that are attributed to C=O (carbonyl and carboxyl) and C-O (epoxy and hydroxyl) groups, respectively. The O1s spectra of M-RGO are deconvoluted to four peaks at 530.2, 531.2, 532.2, and 533.3 eV (Figure 6b). The peaks at 532.2 and 533.3 eV should be referred to the remaining oxygen functionalities of M-RGO. In addition, the emerging peak at 530.2 is attributed to Fe-O bonds in the crystalline structure of Fe_3O_4 NPs. The second peak appearing at 531.2 eV is assigned to C-O-Fe bond formed at high temperature and pressure condition of supercritical methanol.

[Insert Figure 7 about Here]

Proposed Formation Mechanism: Finding an acceptable mechanism that could be accounted for simultaneous formation of Fe_3O_4 NPs, reduction of GO by methanol, and eventually interaction of Fe_3O_4 NPs with graphene or methanol is a formidable task that is evidently out of the scope of the current study. Nevertheless, we tried to summarize the obtained evidence, and address some general guidelines that are helpful for devising such mechanism in future. In this regard, first, the interaction of Fe_3O_4 NPs with graphene sheets investigated using DFT. Then, the interaction of methanol for modifying of Fe_3O_4 NPs surface was studied.

Adsorption of Fe_3O_4 NPs onto graphene surface (Density Functional Theory): In order to find the most stable geometry of graphene-(Fe_3O_4) complexes, we placed (Fe_3O_4) cluster in all possible states on the graphene surface. Then, these structures were optimized at the M06-2X/cc-pVDZ level of theory. The most stable geometry for adsorption of (Fe_3O_4) cluster on the graphene surface is displayed in Figure 8. As it is seen in this Figure, sequestering of Fe_3O_4

cluster on the graphene surface can take place through either iron or oxygen atoms in Fe_3O_4 structure.

[Insert Figure 8 about Here]

Assuming that Fe and O atoms were 2.430 Å and 3.00 Å apart from the graphene surface, the binding energy was determined as the difference between the energy of "G …Fe_3O_4" complex and the sum of the energies of the graphene surface and (Fe_3O_4) cluster ($\Delta E_b = E_{(G\ldots(Fe3O4))} - (E_{((Fe3O4))} + E_{(G)})$). The counterpoise procedure (CP) by Boys and Bernardi was used to calculate the basis set superposition errors (BSSEs)[42] , and then the binding energy for adsorption of (Fe_3O_4) on the graphene surface was corrected by the calculated BSSEs. The calculated binding energy (ΔE_b) was about -14.60 kcal/mol at the M06-2X/cc-pVDZ level of theory.

The energy difference between the Highest Occupied Molecular Orbital (HOMO) and Lowest Unoccupied Molecular Orbital (LUMO) is termed the HOMO-LUMO energy gap. The magnitude of HOMO-LUMO energy gap depends on the relative magnitude of respective orbital energies. The HOMO-LUMO energy gap of graphene surface in our circumcoronene model was about 4.32 eV. With adsorption of the $(Fe_3O_4)_1$ on the graphene surface, the HOMO-LUMO band gap decreased from 4.32 eV to 4.09 eV in "G…Fe_3O_4" complex. Another useful technique for investigating of the changes in the HOMO-LUMO energy gap due to molecular interactions is DOS. Density of state (DOS) of a system describes the number of states per interval of energy at each energy level that are available for occupation by electrons. The DOS spectra for the graphene surface and "G…Fe_3O_4" complex is shown in Figure 9. As seen in this figure, energies of HOMO and LUMO orbitals of graphene shift to more positive values upon adsorption of

Fe_3O_4 on the graphene surface. These changes cause a decrease in HOMO-LUMO energy gap of about 0.23 eV.

[Insert Figure 9 about Here]

In order to evaluate the charge transfer mechanism between Fe_3O_4 cluster and the graphene surface, Mulliken population analysis on the optimized "G…Fe_3O_4" complex was performed at the M06-2X/cc-pVDZ level of theory. Upon adsorption of Fe_3O_4 cluster on the graphene surface, the overall charge on the graphene surface becomes about 0.0236e negative, indicating charge transfer from Fe_3O_4 cluster to the graphene surface. The bond properties between each pair of atoms were systematically analyzed using quantum theory of atoms in molecules (QTAIM)[43]. Based on this theory, electron density ($\rho(r)$) value at the bond critical point (BCP) formed between two atoms is used to describe the strength of a bond, a stronger bond associated with a larger $\rho(r)$ value. The electron density values at the BCPs formed between Fe and O atoms of Fe_3O_4 cluster and graphene surface are 0.0293 and 0.0092, respectively. These values show that the bond formed between Fe and C (Fe-C) is stronger than O and C atom (C-O bond). On the other hand, based on the Bader's theory, the binding energies "$E_{Fe/O...C}$" were calculated using the equation of $E_{Fe/O...C}$ = 1/2V(r) (V(r) = potential energy density at the BCPs).[35] Our calculations showed that the binding energy values for interaction of Fe and O atoms of Fe_3O_4 cluster with graphene surface are -9.08 and -1.89 kcal/mol, respectively.

Surface modification of Fe_3O_4 NPs using methanol: It is important to figure out mechanisms of simultaneous reactions of supercritical methanol with Fe_3O_4 NPs, and the GO. In this regards, FTIR analysis was used to support proposed surface interaction of magnetite nanoparticles and

RGO sheets. As shown in Figure 10, a broad hydroxyl (-OH) stretch bond appeared on the surface of M-RGO, while no peak is detected in RGO. Thus, the aforementioned peak likely refers to the modification of Fe_3O_4 surface with OH groups (Figure 12a). Furthermore, a doublet peak around 2900 cm^{-1} that corresponds to methylene (-CH2-) and methyl (-CH3) asymmetric and symmetric stretching vibrations has become stronger in M-RGO compared to GO and RGO. In addition, intensity of a band around 1037 cm^{-1} assigning to the –C-O stretching vibration increased in comparison with GO and especially RGO. Logically the intensity of –OH and –C-O stretching peaks should be decreased in M-RGO, as it was attenuated in RGO after the SCMeOH treatment. But higher intensity of the aforementioned peaks in M-RGO represents the presence of oxygenated functional groups on the surface of Fe_3O_4 NPs. The three described pieces of evidences reveal that the surface of Fe_3O_4 NPs in M-RGO is covered with hydroxyl (OH) and alkoxide (-C-OH) groups (Figure 12a). The similar effects of supercritical or near critical alcohols on surfaces of ZnO, CeO_2, Al_2O_3, TiO_2, and ZrO_2 nanoparticles were reported previously.[44-46] Combining the results of these reports with our own observations, will lead us to the outcome that methanol acts as a strong hydroxylation and alkoxylation agent at supercritical condition, resulting in surface modification of different NPs.

[Insert Figure 10 about Here]

Another useful tool to study thermal stability of the prepared materials is thermogravimetric analysis. The TG curve (Figure 11) illustrates three major weight loss for GO. The first one, an 8% weight loss occurring up to 110 °C corresponds to the absorbed water on the GO nanosheets. The second weight loss at 225^{o}C (30%) is attributed to the loss of CO and CO_2 due to the decomposition of the oxygenated functional groups. The third and the main weight loss (50%) refers to oxidation of carbon atoms at high temperature and in the presence of the air.

The TG curve of M-RGO hybrid demonstrates just one major weight loss (16%) which is attributed to oxidation of carbon atoms and decomposition of functional groups on the surface of M-RGO. According to wet chemical method, Fe_3O_4 NPs comprise about 92% of M-RGO (Table 1), and the remaining 8% is mainly made of graphene.

[Insert Figure 11 about Here]

Figure 12 proposes a few probable mechanisms for interaction of SCMeOH with Fe_3O_4 NPs according to our FTIR, XPS, and TG experiments, and the results of the previous studies. The first step in these mechanisms is adsorption of methanol on the surface of Fe_3O_4 NPs. If the adsorbed methanol acts as an acid, its hydrogen atom can be connected to oxygen atoms of Fe_3O_4 NPs. Disproportionation of H^+ from methanol leaves the methoxide group with a negative charge, and force it to connect to the surface Fe^{3+} sites of the Fe_3O_4 (Figure 12a). The final outcome is creation of two alkoxide and hydroxide groups on the surface of Fe_3O_4 NPs as it is shown in Figure 12a and Figure S8a. According to the FTIR spectra, carboxylic acid peak (1740 cm-1) disappeared in M-RGO, while a new peak at 1540 cm^{-1} assigning to carboxylate emerged. Such a species formation was formerly recognized by Idriss and co-workers.[47] Furthermore, according to Zaki and co-workers, with increasing of temperature in supercritical alcohols, the absorbed alkoxides groups undergo a dehydrogenation process that is followed by demethylation in the next step.[48] The aforementioned dehydrogenation-demethylation reactions are completed by the consequent formation of the bridged carboxylate species on the surface of Fe_3O_4 as it shown in Figure 12b and Figure S8b. It can be observed in Figure 12c and Figure S8c that chelating type carboxylate is possibly formed using two successive dehydrogenation processes.

[Insert Figure 12 about Here]

Adsorption properties

Adsorption capacity. The adsorption capacities of RGO, Fe_3O_4 NPs and M-RGO for $Sr^{2+}$and Co^{2+} ions were obtained by undertaking the batch experiments, and drawing of the adsorption isotherms.

According to Figure 13a and b, adsorption capacity of M-RGO for Co^{2+} ions was about two folds higher than the Sr^{2+} ions, possibly due to the greater affinity of Fe_3O_4 NPs toward the Fe(II)-like cations.[16] In other words, the close similarity between the cobalt and iron ions allows a more effective sequestering of Co^{2+} ions on Fe_3O_4 by ion exchange or other mechanisms. To prove this argument, adsorption ability of pure Fe_3O_4 NPs toward $Sr^{2+}$and Co^{2+} ions was examined and depicted in Figures 13 a, and b. In contrast to the RGO whose maximum adsorption capacity for both of $Sr^{2+}$and Co^{2+} ions is nearly identical (Figures 13 a, and b), the Fe_3O_4 NPs show much higher affinity toward Co^{2+} ions.

The aforementioned Fe_3O_4 NPs were prepared in SCMeOH medium and thus were rich in different functional groups such as hydroxyl, alkoxide, and carboxylate on their surfaces (Figure 12). Existence of such oxygen functionalities enhances the adsorption capacity of Fe_3O_4 NPs appreciably, and gives an evident advantage to those particle in comparison to the Fe_3O_4 NPs which are prepared by ultrasound method in aqueous media[16] (Figure S9)

Another significant phenomenon which is observed in Figures 13 a-d, is the higher adsorption capacity of M-RGO in comparison to both of the RGO and Fe_3O_4 NPs. According to the wet chemical analysis and the TG method, the M-RGO nanocomposite comprises of 92% wt. Fe_3O_4 and 8% wt RGO. Thus, it is expected to have an adsorption capacity equal to the arithmetic mean of the adsorption capacities of its constituents. Surprisingly, this is not true, and the actual behavior of M-RGO displays a synergetic effect in adsorption of Sr^{2+} and Co^{2+} ions. This interesting phenomenon can be explained by using the discussions of the last paragraph as

follows: As it was shown, not body of the Fe_3O_4 NPs, but indeed their active surfaces is responsible for the uptake of the metal ions. As a result, any factor that causes agglomeration of the Fe_3O_4 NPs, will lead to reducing of their uptake ability. The M-RGO and pure Fe_3O_4 NPs both were synthesized in methanol medium, and thus both must have been rich in surface functional groups. However, as the TEM images reveal (Figure S10) the pure Fe_3O_4 NPs are agglomerated, while the M-RGO is consisted of the Fe_3O_4 NPs that are homogenously and separately distributed on the surface of graphene sheet (Figures S10 b). As was discussed in the morphology section, the huge surface area and numerous active site of graphene oxide as a starting materials causes homogenous dispersion of Fe_3O_4 NPs and inhibits agglomeration of them.

[Insert Figure 13 about here]

In order to achieve more information about the adsorption mechanisms, the Langmuir and Freundlichs' models were fitted on the experimental data. The Langmuir model is expressed by:

$$Q_e = \frac{bQ_{\max}C_e}{1+bC_e} \qquad (7)$$

The Freundlich model is represented by the following equation:

$$Q_e = KC_e^n \qquad (8)$$

where Q_{max}(mmol.g^{-1}) denotes maximum adsorption capacity, Q_e(mmol.g^{-1}) shows the equilibrium loading on the adsorbent, C_e(ppm) stands for equilibrium concentration of ions in solution, and b(L.mg^{-1}), K and n are the empirical constants that depend on the nature of ions and the adsorbent. The experimental data for adsorption of Sr^{2+} and Co^{2+} ions on the M-RGO were

regressively simulated with Langmuir and Freundlichs' models (Figure 13c and d), and the corresponding fitting parameters were listed in Tables 2 and 3. It can be inferred from the correlation coefficients R^2 and fitting curves (Figure 13c and d) that the Langmuir's model provides a better fitting than the Freundlich, and hence, monolayer coverage of the adsorbent surface according to the Langmuir's model, appears to be the main adsorption mechanism. This result fairly agrees with our previous conclusion that the not body of the Fe_3O_4 NPs, but indeed their active surfaces is responsible for major portion of the uptake process.

According to Tables 2 and 3, the higher is the temperature, the greater is the adsorption capacity of the M-RGO. For the Co^{2+} and Sr^{2+} ions, the maximum achieved values of the Q_{max} were equal to 1.1 and 0.6 $mmol.g^{-1}$, respectively that were obtained at 338 K. Interestingly, the maximum adsorption capacity of M-RGO is two times greater than that for M-GO which indicates the positive effect of SCMeOH in increasing of the acidic (-COOH) as well as hydroxyl (-OH) groups on the surface of Fe_3O_4 NPs which results in higher affinity toward the metal cations.

[Insert Table 2 about here]

[Insert Table 3 about here]

Thermodynamic parameters such as ΔG^0, ΔH^0, ΔS^0 provide valuable information about the endothermic or exothermic nature of the reaction and its degree of spontaneity. These parameters can be estimated from temperature-dependent uptake data by the following equations:

$$\Delta G^0 = -RTLnK^0 \qquad (9)$$

$$\frac{\partial\left(\frac{\Delta G^0}{T}\right)}{\partial T} = -\frac{\Delta H^0}{T^2} \qquad (10)$$

$$\Delta G^0 = \Delta H^0 - T\Delta S^0 \qquad (11)$$

where K^0 is the uptake equilibrium constant. Having plotted LnK_d curves versus C_e (Figure S11 in supplementary information) and extrapolating C_e to zero, Ln K^0 values can be obtained for every temperature. The Ln K^0 values then are used for calculation of ΔG^0 using eq. (10). Thereafter, the $\frac{\Delta G^0}{T}$ values, which are obtained from Ln K^0, can be re-plotted against $\frac{1}{T}$to result in the ΔH^0 by application of eq. (11) on their line slopes. (Figure S12 in supplementary information). Also, the entropy difference ΔS^0 is obtained from eq. (12).

The results of calculation of the above thermodynamic parameters are presented in Table 4. The positivity of the ΔH^0 values reveals endothermic nature of the sorption process. This result is in a good agreement with the previous observation about improving of the maximum uptake rate (i.e. Q_{max}) with increasing of the temperature.

[Insert Table 4 about here]

Adsorption kinetics. Kinetics experiments indicate attaining 90% equilibrium level within 60 min (Figure 14a). In addition from normalized kinetics data, it can be realized that, Co^{2+} always presents a faster kinetics than Sr^{2+} (Figure S13). This phenomenon is probably arisen from similarity in the size and nature of the cobalt ions with the iron atoms initially existing in the magnetite NPs which have been reported for Sr^{2+} and Co^{2+} and some other metal oxides by our group previously[16].

In order to acquire information regarding to kinetics data and find out the rate controlling step of the kinetics, two different kinds of kinetics models were utilized.

First, the kinetics data were fitted with pseudo second order reaction model, represented by:

$$\frac{t}{Q_t} = \frac{1}{K_2 Q_e^2} + \frac{t}{Q_e} \qquad (12)$$

where K_2 ($g.mg^{-1}.min^{-1}$) is the ion-specific rate constant, Q_t ($mg.g^{-1}$) is the amount of Co^{2+} and Sr^{2+} ions adsorbed into M-RGO at time t(min), and Qe ($mg.g^{-1}$) is the adsorption capacity at equilibrium. Figure 14b shows that the correlation coefficient R^2 is very close to 1, indicating remarkable fitting of the data for both Co^{2+} and Sr^{2+} ions.

Furthermore, the kinetics data were fitted using the well-known shrinking core model (SCM).[49] There are three different types of SCM which are liquid film resistance, intraparticle resistance, and the reaction control one. Mathematically, these are represented by the following formulae:

$$X = \frac{3D}{C^0 R\delta}\int_0^t C\,dt \qquad \text{Liquid film resistance} \qquad (11)$$

$$1-3(1-X)^{2/3}+(1-X) = \frac{6D_e}{C^0 R^2}\int_0^t C\,dt \qquad \text{Intraparticle resistance} \qquad (12)$$

$$1-(1-X)^{1/3} = \frac{k''}{\rho R}\int_0^t C\,dt \qquad \text{Reaction-controlled kinetics} \qquad (13)$$

where "X" is fractional attainment to the equilibrium and C (ppm) is concentration at any given time of t, D ($cm^2.s^{-1}$) and De ($cm^2.s^{-1}$) denote diffusion rates of liquid film and Fe_3O_4 NPs, respectively. Also, R (cm) stands for the radius of the particles, and δ (cm) shows the thickness of liquid film. Other parameters include C_0 the concentration of active sites of the adsorbent ($mmol/dm^{-3}$), ρ (g/cm^3) as its density and finally k" the rate constant of adsorption reaction. Here, the best fitting of the kinetics data was provided by chemical reaction (Figure 14c and d). This implies that the rate determining step is chemical reaction between ions and M-RGO.

[Insert Figure 14 about Here]

Besides the abovementioned fitting results, there are three pieces of evidence that show the rate determining step of the adsorption is more likely chemical reaction of the ions with M-RGO hybrid. 1: Nano sized magnetite or graphene particles cannot present intraparticle resistance, 2: Uptake kinetics greatly depends to the nature of ions so that for Co^{2+} is about two times faster Indeed in a series of experiment that were conducted on adsorption of Th^{4+} ions by graphene oxide, the present authors observed an instantaneous rate of adsorption. This facet reveals the importance of the nature of the ion or in other word the role of chemical reaction in kinetics 3: The Diffusion coefficient of Sr^{2+} ion in water which is about 7.9×10^{-6} cm^2/s is higher than 6.5×10^{-6} cm^2/s of Co^{2+}, thus if liquid film resistance had been the rate controlling factor, adsorption of Sr^{2+} ions should take place faster than the Co^{2+}.

Effect of the pH. Concentration of H^+ ions (pH) plays an important role in determining the rate of adsorption of Sr^{2+} and Co^{2+} ion either by changing the surface charge of the adsorbent, or altering the nature of the ion species in the solution. In particular, comparison between uptake properties of M-RGO with the magnetite graphene hybrid (M-GO) synthesized under ultrasound radiation, could reveal the effect of supercritical surface modification of methanol medium on the adsorption of ions. Due to electrostatic nature of the adsorption of Sr^{2+} and Co^{2+} ions on the surface of M-RGO, it was important to find, and compare the points of zero charge (PZC) of M-RGO and M-GO hybrid as a function of pH. As it is discussed in a previous publication,[16] Fe_3O_4 NPs deposited on the surface of GO by ultrasound-assisted method have an average size of 17 nm, which is very close to the size magnetite NPs in M-RGO (dav= 15 nm). Figure 15 shows the surface charge of both M-RGO and M-GO as a function of pH. According to this figure: 1. Point of zero charge for M-RGO (pH_{PZC}=1.9) emerges at lower pHs than M-GO (pH_{PZC}=3.7). This

phenomenon can be attributed to the presence of larger number of anions like hydroxide, alkoxide and carboxylate on the surface of M-RGO, which needs lower pH (higher concentration of H^+ ions) to neutralize all negative charges and allows changing of the sign of surface charge from negative to positive, 2. A typical adsorbent at pHs<pH_{ZCP}, acquire positive surface charge and consequently acts as an anion exchanger; but at pH>pH_{ZCP}, the surface charge turns into negative and thus, adsorbent favors adsorption of cations (e.g. Sr^{2+} and Co^{2+} ions). Since pH_{ZCP} for M-RGO is lower than M-GO, the M-RGO indicates higher adsorption ability in acidic media than M-GO that is considered as a merit for the former.

[Insert Figure 15 about Here]

Figure 16 displays uptake percentage of Co^{2+} and Sr^{2+} ions onto M-RGO hybrid. Adsorption capacity of M-RGO for Co^{2+} ions in whole range of pH is higher than M-GO as a result of: 1- The presence of more abundant active sites and functional groups on the surface of the M-RGO (Figure 12) which is result of the surface modification of Fe_3O_4 NPs by supercritical methanol medium, and 2- Higher Fe_3O_4 NPs content in M-RGO (92% wt.) in comparison with M-GO (58% wt.) which play an important role in adsorption of Sr^{2+} and Co^{2+} ions.

For M-GO, the uptake percentage remains quit small up to pH≈5, while in the case of M-RGO this break point occurs at lower pH (pH≈2.1). This behavior is attributed to emerging of PZC for M-RGO at lower pH (pH=1.9) compared to PZC of M-GO (pH=3.7). Taking into consideration, the simplicity of magnetic separation of M-RGO from the solution (Figure S1), and high adsorption capacity in acidic solutions, the M-RGO appears to be a promising material for removal of toxic cations from industrial effluents.

[Insert Figure 16 about here]

Desorption Behavior and Reusability: Any adsorbent that is supposed to be employed in the practical separation processes should be desorbed in an inexpensive scheme, using a commercially available eluent. As for finding an appropriate eluent, we examined different concentration of hydrochloric acid, and represented the results in the bar type chart of Figure S14. The best stripping effect was obtained by 0.5M and 1M solutions for both Sr^{2+} and Co^{2+} ions.

Another important characteristic of a commercial adsorbent which reduces operational cost of the adsorption process is reusability, meaning that the uptake capacity should be maintained in the successive adsorption-desorption cycles. As the outcome of the experiments of the last paragraph, we exploited a solution of 0.5 M HCl for elution, and conducted a 4-cycle adsorption-desorption test on the prepared samples. The obtained data in Figure 17 a reveals that M-GO losses around 30% and 25% of its initial capacity for Sr^{2+} and Co^{2+} ions after four cycles of adsorption, respectively. In contrast, M-RGO could keep its adsorption capacity nearly intact even after four cycles of adsorption-desorption (Figure 17b). This could be attributed to numerous functional groups such as hydroxyl, alkoxide, and carboxylate on Fe_3O_4 NPs surfaces (Figure 12) resulted in retaining the adsorption capacity of M-RGO in comparison with M-GO. These experiments clearly demonstrate the superiority of the M-RGO hybrid over the M-GO in practical separation of Sr^{2+} and Co^{2+} ions.

[Insert Figure 17 about Here]

Conclusion: A green, quick, and flexible method for simultaneous synthesis and grafting of the Fe_3O_4 NPs onto surface of graphene was introduced in the current study. Supercritical methanol in which such fabrication process was conducted, provides a unique reaction medium that

supports both reduction of GO, and surface modification of Fe_3O_4 NPs by alkoxides, hydroxyl, and carboxylate groups.

The result of different instrumental analyses and a theoretical density functional simulation allowed us to propose a formation mechanism for M-RGO hybrid according to which, 1- After grafting of magnetite nanoparticles onto the surface of graphene, the overall surface charge becomes about 0.0236e negative, exhibiting a charge transfer from Fe_3O_4 cluster to graphene surface. In addition, it was shown that Fe_3O_4 cluster is connected to the surface of graphene via C-O-Fe and C-Fe bonds, 2- Supercritical methanol significantly modifies surface of Fe_3O_4 NPs by negative functional groups, and results in higher adsorption affinity toward Co^{2+} and Sr^{2+} ions.

As a result of the aforementioned surface modification, adsorption capacity of M-RGO is appreciably a higher than the previously synthesized ultrasound-assisted M-GO composite. Due to the similarity of Co^{2+} and Fe^{2+} ions, the uptake capacity of M-RGO for Co^{2+} ion was about two folds higher than Sr^{2+} ion, but for both of the ions, uptake isotherm closely followed Langmuir's monolayer model, with the maximum capacity of 1.1 and 0.6 mmol/g Co^{2+} and Sr^{2+}, respectively.

The kinetics data were modeled by different forms of shrinking core model. The results showed that for both Co^{2+} and Sr^{2+} ions, chemical reaction SCM provided the best fitting. Furthermore, the adsorption kinetics obeyed pseudo-second-order reaction model for both of the studied ions, indicating that the chemical reaction of ions with the functional groups on the surface of M-RGO is the rate controlling step of the adsorption.

Thermodynamic data indicated that adsorption of both of the Sr^{2+} and Co^{2+} ions was endothermic, and entropy slightly increased during the adsorption process.

Examining of the pH-dependent sorption of the Sr^{2+} and Co^{2+} ions, along with Zeta potential measurement, exhibited that by increasing of the pH, surface charge of the M-RGO changes from positive to negative at pH_{PZC} =1.9, and consequently, adsorption ability for metal cations initiate at pH>2, even though abrupt jump in adsorption ability takes place at pHs>4. Reusability tests indicated that M-RGO hybrid could be used in at least 4 cycles of adsorption-desorption process without considerable losses of the capacity. Therefore, M-RGO could be considered as a promising alternative of the well-known magnetite-graphene oxide hybrid in uptake of heavy metal ions from the aqueous solutions.

References:

1 F. K. Shieh, C.-T. Hsiao, H.-M. Kao, Y.-C. Sue, K.-W. Lin, C.-C. Wu, X.-H. Chen, L. Wan, M.-H. Hsu and J. R. Hwu, *RSC Advances*, 2013, **3**, 25686-25689.

2 V. K. Gupta, I. Ali, T. A. Saleh, A. Nayak and S. Agarwal, *RSC Advances*, 2012, **2**, 6380-6388.

3 S. Pollard, G. Fowler, C. Sollars and R. Perry, *Sci. Total Environ.*, 1992, **116**, 31-52.

4 K. A. Mkhoyan, A. W. Contryman, J. Silcox, D. A. Stewart, G. Eda, C. Mattevi, S. Miller and M. Chhowalla, *Nano lett.*, 2009, **9**, 1058-1063.

5 W. Gao, L. B. Alemany, L. Ci and P. M. Ajayan, *Nat. chem.*, 2009, **1**, 403-408.

6 Y. K. Kim, H. K. Na, S. Kim, H. Jang, S. J. Chang and D. H. Min, *Small*, 2015.

7 S. Dutta, C. Ray, S. Sarkar, M. Pradhan, Y. Negishi and T. Pal, *ACS Appl. Mater. Inter.*, 2013, **5**, 8724-8732.

8 C. Nethravathi, E. Anumol, M. Rajamathi and N. Ravishankar, *Nanoscale*, 2011, **3**, 569-571.

9 P. Fernández-Ibáñez, M. Polo-López, S. Malato, S. Wadhwa, J. Hamilton, P. Dunlop, R. D'Sa, E. Magee, K. O'Shea and D. Dionysiou, *Chem. Eng. J.*, 2015, **261**, 36-44.

10 S. Moradi, O. Akhavan, A. Tayyebi, R. Rahighi, M. Mohammadzadeh and H. S. Rad, *RSC Advances*, 2015, **5**, 47529-47537.

11 M. Srivastava, J. Singh, T. Kuila, R. K. Layek, N. H. Kim and J. H. Lee, *Nanoscale*, 2015, **7**, 4820-4868.

12 A. K. Swain, L. Pradhan and D. Bahadur, *ACS Appl. Mater. Inter.*, 2015, **7**, 8013-8022.

13 G. Bharath, V. Veeramani, S.-M. Chen, R. Madhu, M. Manivel Raja, A. Balamurugan, D. Mangalaraj, C. Viswanathan and N. Ponpandian, *RSC Advances*, 2015, **5**, 13392-13401.

14 R. Justin, K. Tao, S. Román, D. Chen, Y. Xu, X. Geng, I. M. Ross, R. T. Grant, A. Pearson, G. Zhou, S. MacNeil, K. Sun and B. Chen, *Carbon*, 2016, **97**, 54-70.

15 J. C. Spear, J. P. Custer and J. D. Batteas, *Nanoscale*, 2015.

16 A. Tayyebi, M. Outokesh, S. Moradi and A. Doram, *Appl. Surf. Sci.*, 2015, **353**, 350-362.

17 T. Qi, C. Huang, S. Yan, X.-J. Li and S.-Y. Pan, *Talanta*, 2015, **144**, 1116-1124.

18 M. Faraji, Y. Yamini and M. Rezaee, *J. Iran. Chem. Soc.*, 2010, **7**, 1-37.

19 B. Veriansyah, J.-D. Kim, B. K. Min and J. Kim, *Mater. Lett.*, 2010, **64**, 2197-2200.

20 A. Baiker, *Chem. Rev.*, 1999, **99**, 453-474.

21 T. Adschiri, Y. Hakuta and K. Arai, *Ind. Eng. Chem. Res.*, 2000, **39**, 4901-4907.

22 C. Xu and A. S. Teja, *J. Super. Fluids*, 2006, **39**, 135-141.

23 D. T. Sawyer and J. L. Roberts Jr, *Accounts Chem. Res.*, 1988, **21**, 469-476.

24 H. Choi, B. Veriansyah, J. Kim, J.-D. Kim and J. W. Kang, *J. Super. Fluids*, 2010, **52**, 285-291.

25 J. Kim, D. Kim, B. Veriansyah, J. W. Kang and J.-D. Kim, *Mater. Lett.*, 2009, **63**, 1880-1882.

26 B. Veriansyah, J.-D. Kim, B. K. Min, Y. H. Shin, Y.-W. Lee and J. Kim, *J. Super. Fluids*, 2010, **52**, 76-83.

27 A. Hadi, J. Karimi-Sabet, S. M. A. Moosavian and S. Ghorbanian, *J. Super. Fluids*, 2015.

28 A. Tayyebi, M. M. Tavakoli, M. Outokesh, A. Shafiekhani and A. Simchi, *Ind. Eng. Chem Res.*, 2015, **54**, 7382-7392.

29 B. Li and H. Cao, *j. Mater. Chem.*, 2011, **21**, 3346-3349.

30 P. T. Yin, S. Shah, M. Chhowalla and K.-B. Lee, *Chem. Rev.*, 2015, **115**, 2483-2531.

31 Y. Shao, J. Wang, H. Wu, J. Liu, I. A. Aksay and Y. Lin, *Electroanalysis*, 2010, **22**, 1027-1036.

32 N. Song, H. Fan and H. Tian, *Appl. Surf. Sci.*, 2015, **353**, 580-587.

33 P. V. Kamat, *J. Phys. Chem. Lett.*, 2010, **1**, 520-527.

34 W. S. Hummers and R. E. Offeman, *J. Am. Chem. Soc.*, 1958, **80**, 1339-1339.

35 M. Shakourian-Fard, Z. Jamshidi, A. Bayat and G. Kamath, *J. Phys. Chem. C*, 2015, **119**, 7095-7108.

36 Y. Zhao and D. G. Truhlar, *Theor. Chem. Acc.*, 2008, **120**, 215-241.

37 R. A. Gaussian09, *Inc., Wallingford CT*, 2009.

38 A. Nourmohammadi, R. Rahighi, O. Akhavan and A. Moshfegh, *J. Alloy. Compd.*, 2014, **612**, 380-385.

39 M. Mahmoudi, A. Simchi, M. Imani, A. S. Milani and P. Stroeve, *J. Phys. Chem. B*, 2008, **112**, 14470-14481.

40 M. Tayebi, S. Ramazani, M. Hamed Mosavian and A. Tayyebi, *Polym. Advan. Technol.*, 2015.

41 M. M. Tavakoli, A. Tayyebi, A. Simchi, H. Aashuri, M. Outokesh and Z. Fan, *J. Nanopart. Res.*, 2015, **17**, 1-13.

42 S. F. Boys and F. d. Bernardi, *Mol. Phys.*, 1970, **19**, 553-566.

43 R. F. Bader, *Atoms in molecules*, Wiley Online Library, 1990.

44 H. Idriss and E. Seebauer, *J. Mol. Catal. A: Chem.*, 2000, **152**, 201-212.

45 C. d. Slostowski, S. Marre, O. Babot, T. Toupance and C. Aymonier, *Langmuir*, 2012, **28**, 16656-16663.

46 M. Hasan, M. Zaki and L. Pasupulety, *J. Mol. Catal. A: Chem.*, 2002, **178**, 125-137.

47 H. Idriss, *Platin. Met. Rev.*, 2004, **48**, 105-115.

48 M. I. Zaki and N. Sheppard, *J. Catal.*, 1983, **80**, 114-122.

49 A. Tayyebi, A. Khanchi, M. Ghofrani and M. Outokesh, *Sep. Sci. Technol.*, 2010, **45**, 288-298.

Figures caption

Figure 1: (a) A typical AFM image of GO sheet on mica and below corresponding height profile analysis of marked-line, and (b) UV-visible absorption of GO, RGO, and M-RGO in aqueous solution (0.01 mg/ml).

Figure 2: (a) Low magnification TEM image of GO, (b) RGO, and (c) M-RGO; Inset figures demonstrate corresponding SAED patterns of prepared materials.

Figure3: (a) SEM image of M-RGO hybrid, (b) Low magnification TEM image of M-RGO, and (c) High Resolution TEM image of Fe_3O_4 NPs synthesized in supercritical methanol.

Figure4: Dynamic light- scattering **(**DLS) of GO, RGO, and M-RGO in aqueous solution.

Figure 5: Magnetization behaviors of Fe3O4 NPs and M-RGO at room temperature, top inset shows close view of the hysteresis loops, and down inset exhibits separation of the M-GO hybrid from its dispersion in water by a simple magnet.

Figure 6: (a) The full scan XPS survey of GO, RGO, and M-RGO, C1s spectra of (b) GO, (c) RGO, and (d) M-RGO.

Figure 7: O1s spectra of (a) GO, and (b) M-RGO.

Figure 8: The most stable geometry for adsorption of $(Fe_3O_4)_1$ cluster on the graphene surface optimized at the M06-2X/cc-pVDZ level of theory.

Figure 9: Density of states of RGO compared to M-RGO.

Figure 10: FTIR spectra of GO, RGO, and M-RGO.

Figure 11: Thermogravimetry analysis (TGA) of GO and M-RGO.

Figure 12: One of the possible pathways for simultaneous interaction of methanol with Fe_3O_4 NPs surface.

Figure 13: Adsorption isotherms of (a) Co^{2+}, (b) Sr^{2+} ions onto RGO, Fe_3O_4 NPs and M-RGO hybrid, the effect of temperature on adsorption capacity of M-RGO for (c) Co^{2+}, and (d) Sr^{2+} ions. **Figure 14:** (a) Rate of adsorption of Co^{2+} and Sr^{2+} ions onto M-RGO hybrid, fitting of adsorption data to the (b) pseudo-second order kinetics model, Shrinking core model for (c) Co^{2+} and (d) Sr^{2+} ions in aqueous solution.

Figure 15: Zeta potential of M-GO and M-RGO versus pH.

Figure 16: The effect of pH on adsorption of M-GO and M-RGO for (a) Co^{2+}, and (b) Sr^{2+} ions from aqueous solution.

Figure 17: Reusability of Co^{2+} and Sr^{2+} ions onto (a) M-GO, and (b) M-RGO (Black= Co^{2+}, Red=Sr^{2+}).

Table 1: Magnetite nanoparticles size estimation using Langevien equation.

Sample	M_S	Mass fraction of Fe_3O_4	$D_{Theoretical}$ (nm) from eq. (5)	$D_{Experimental}$(nm)
M-RGO	60	0.92	19	15 (Figure S3)
Magnetite (Fe_3O_4)	76	1	27	25 (Figure S5)

Table 2: Parameters of Langmuir and Freundlich isotherm model for Co^{2+} ions at pH 6.5 (±0.2) at different temperature.

	Langmuir			Freundlich		
T (K)	Q_{max}(mmol.g^{-1})	b(L.mmol^{-1})	R^2	K_2	n	R^2
298	0.71	0.21	0.99	15	0.28	0.9
318	0.9	0.32	0.99	16.7	0.31	0.89
338	1.1	0.24	0.97	22	0.33	0.83

Table 3: Parameters of Langmuir and Freundlich isotherm model for Sr^{2+} ions at pH 6.5(±0.2) at different temperature.

	Langmuir			Freundlich		
T (K)	Q_{max}(mmol.g^{-1})	b(L.mmol^{-1})	R^2	K_2	n	R^2
298	0.36	0.15	0.95	10	0.28	0.82
318	0.5	0.27	0.96	16	0.26	0.84
338	0.6	0.64	0.95	26	0.21	0.79

Table 4: Values of Thermodynamic Parameters for Co^{2+} and Sr^{2+} Sorption on the M-RGO.

Ions	ΔG^0 (kj.mol^{-1})			ΔS^0 (kj.mol^{-1} K^{-1})	ΔH^0 (kj.mol^{-1})
	298	318	338		
Co^{2+}	-4.2	-4.9	-5.9	0.1	14.2
Sr^{2+}	-2.4	-3.9	-5.8	0.1	10.7

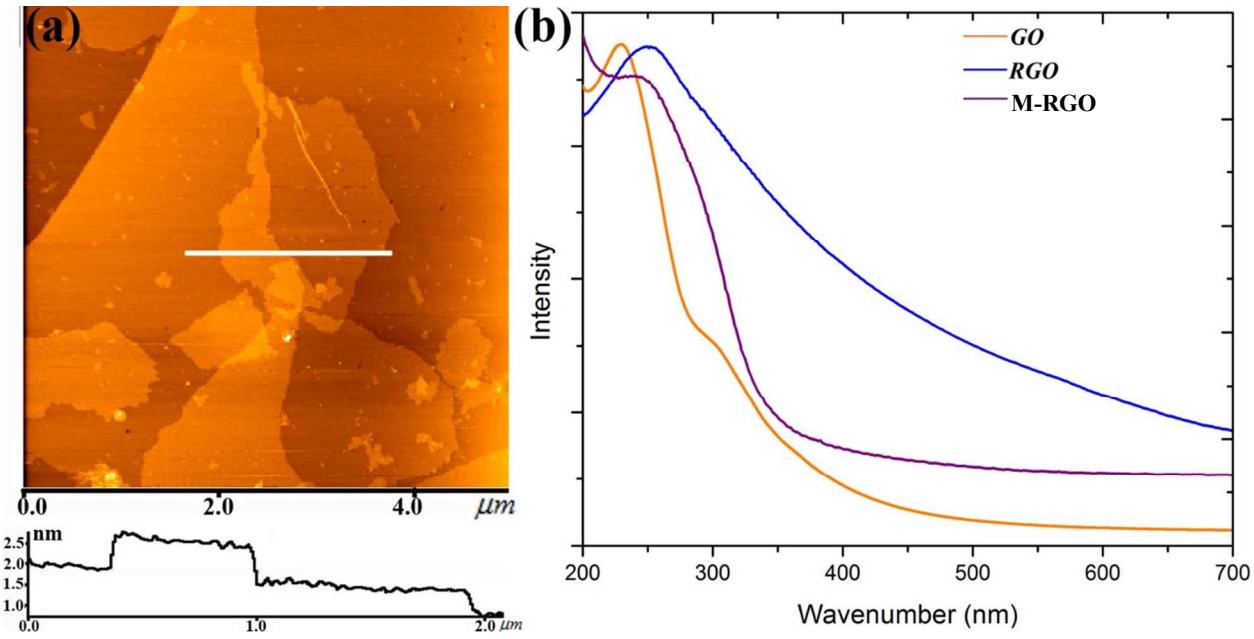

Figure 1: (a) A typical AFM image of GO sheet on mica and below corresponding height profile analysis of marked-line, and (b) UV-visible absorption of GO, RGO, and M-RGO in aqueous solution (0.01 mg/ml).

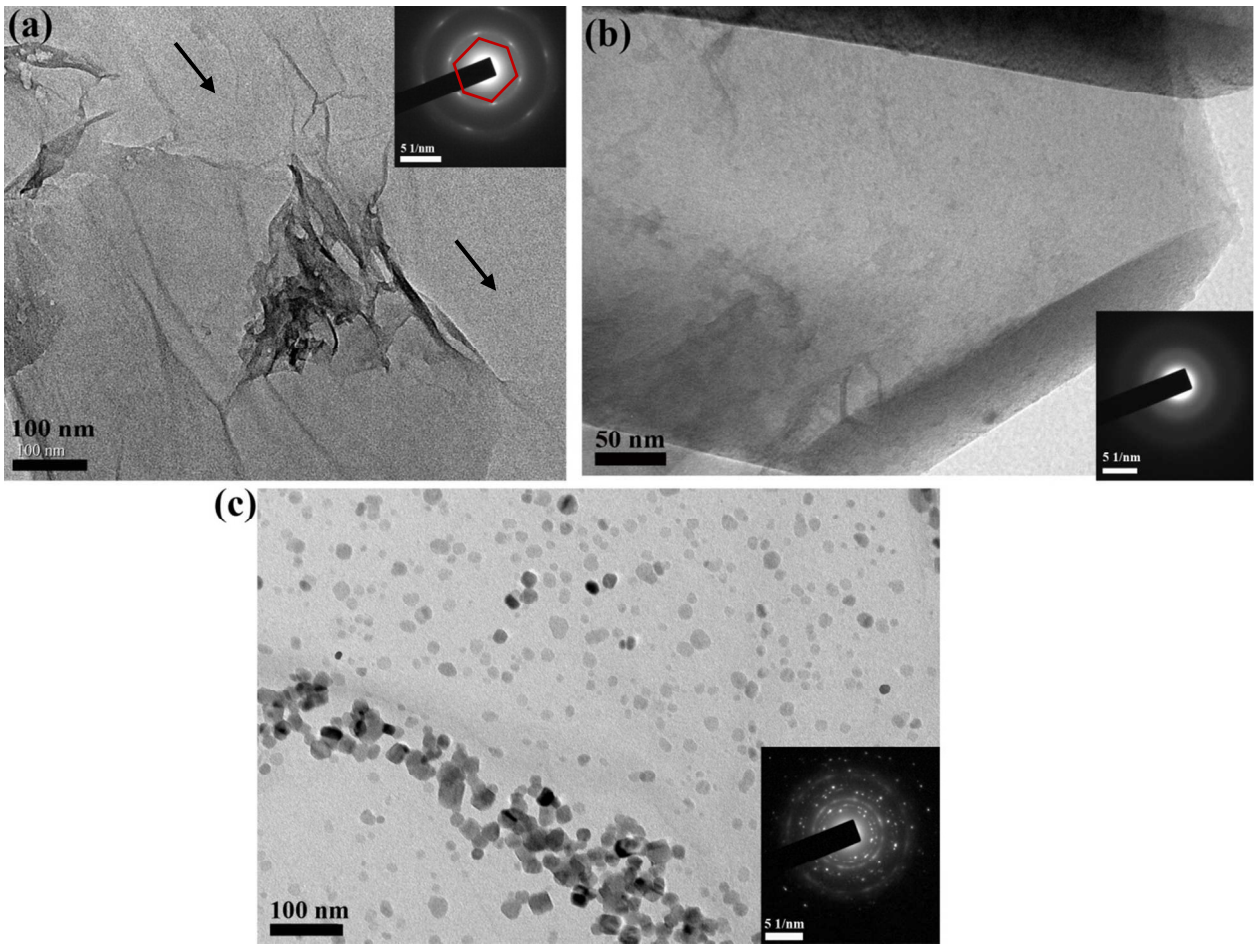

Figure 2: (a) Low magnification TEM image of GO, (b) RGO, and (c) M-RGO; Inset figures demonstrate corresponding SAED patterns of prepared materials.

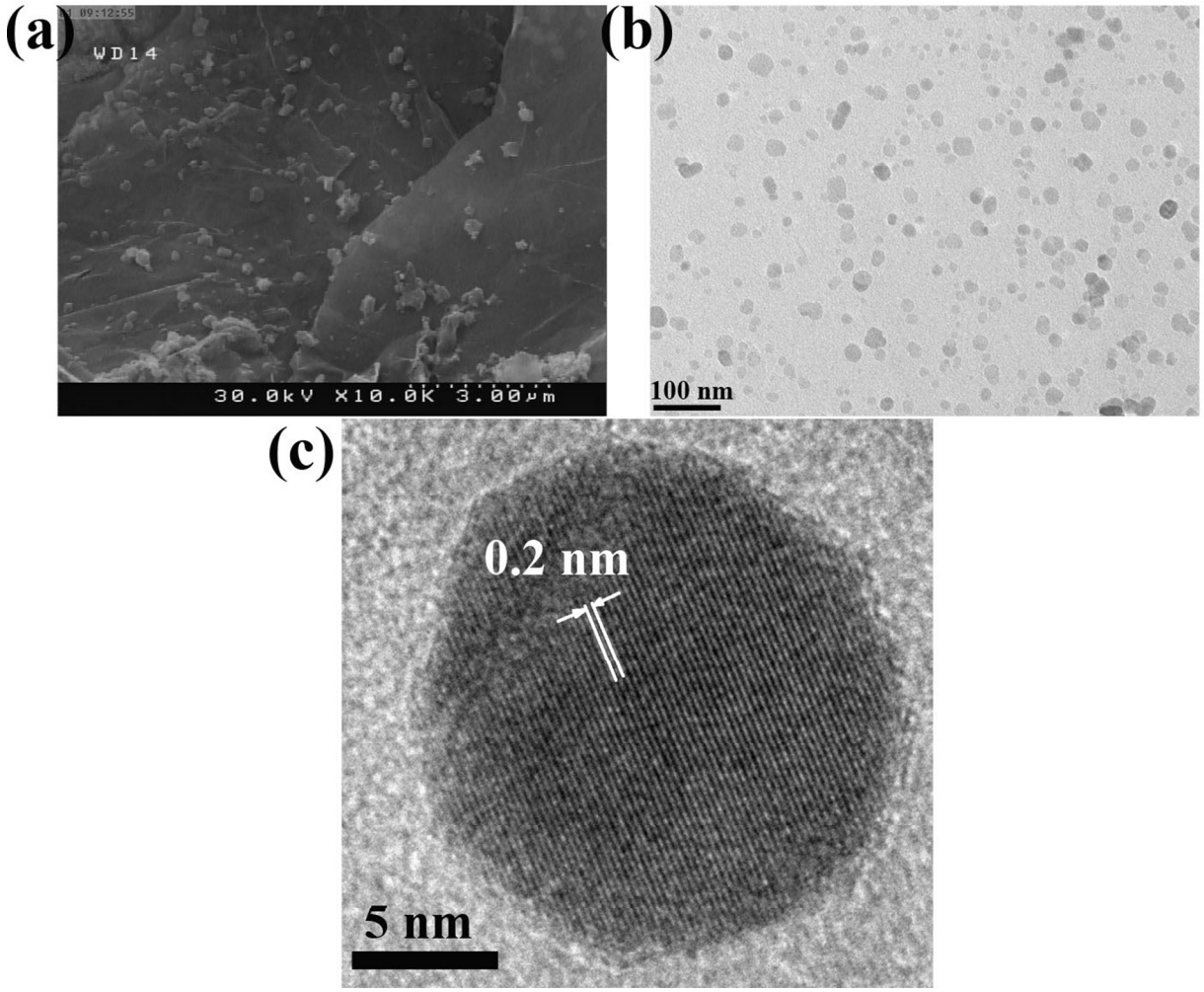

Figure3: (a) SEM image of M-RGO hybrid, (b) Low magnification TEM image of M-RGO, and (c) High Resolution TEM image of Fe_3O_4 NPs synthesized in supercritical methanol.

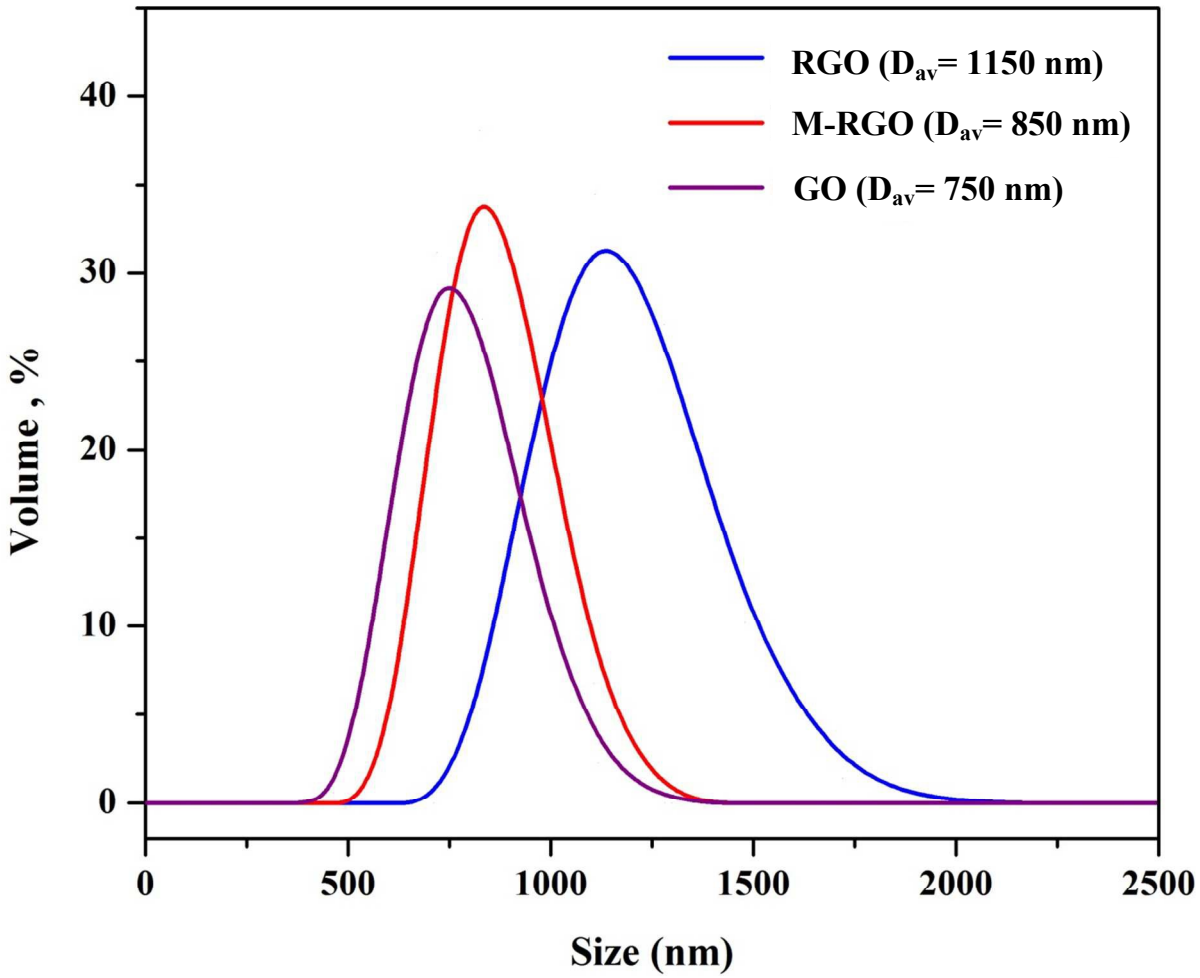

Figure4: Dynamic light- scattering (DLS) of GO, RGO, and M-RGO in aqueous solution.

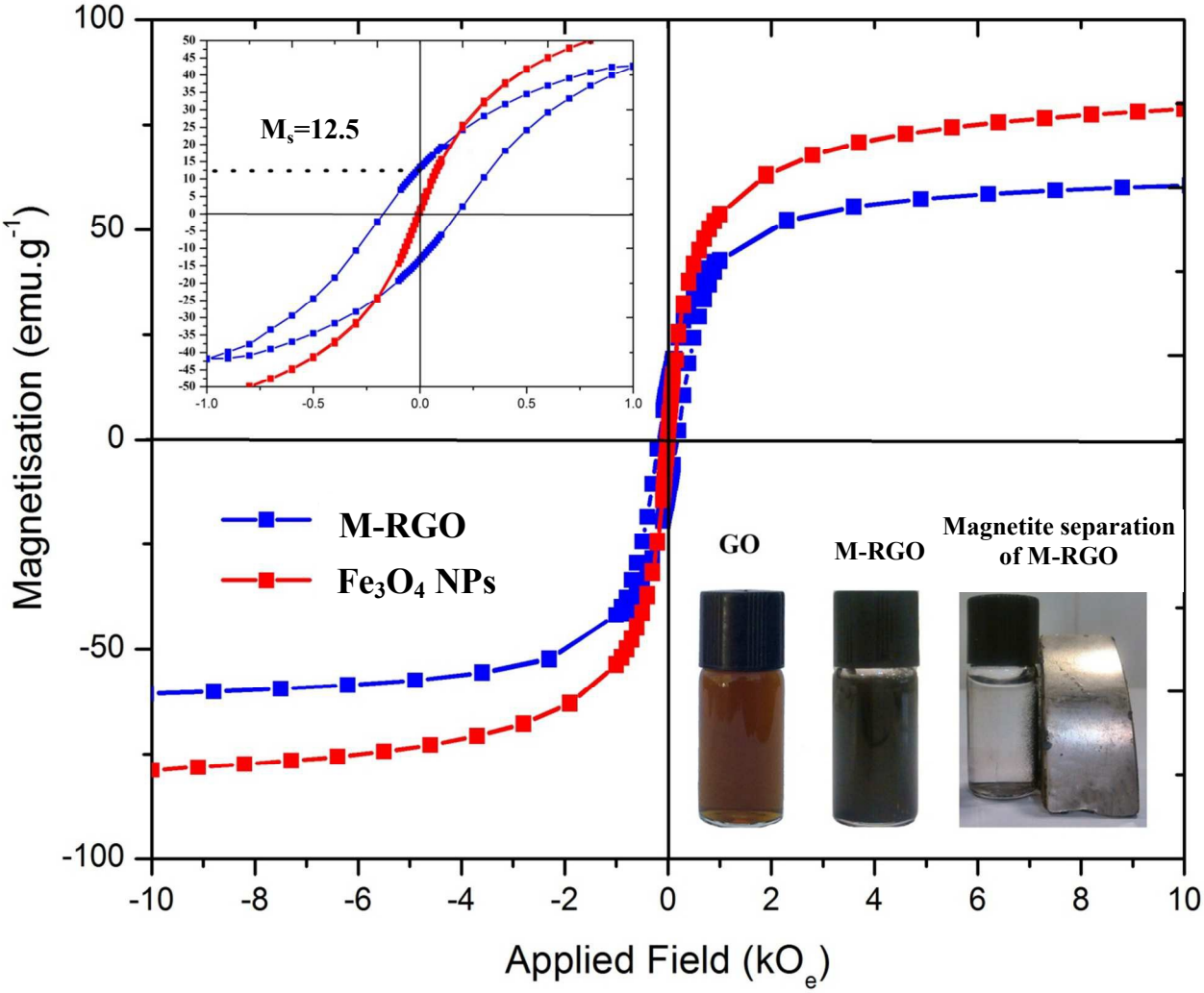

Figure 5: Magnetization behaviors of Fe3O4 NPs and M-RGO at room temperature, top inset shows close view of the hysteresis loops, and down inset exhibits separation of the M-GO hybrid from its dispersion in water by a simple magnet.

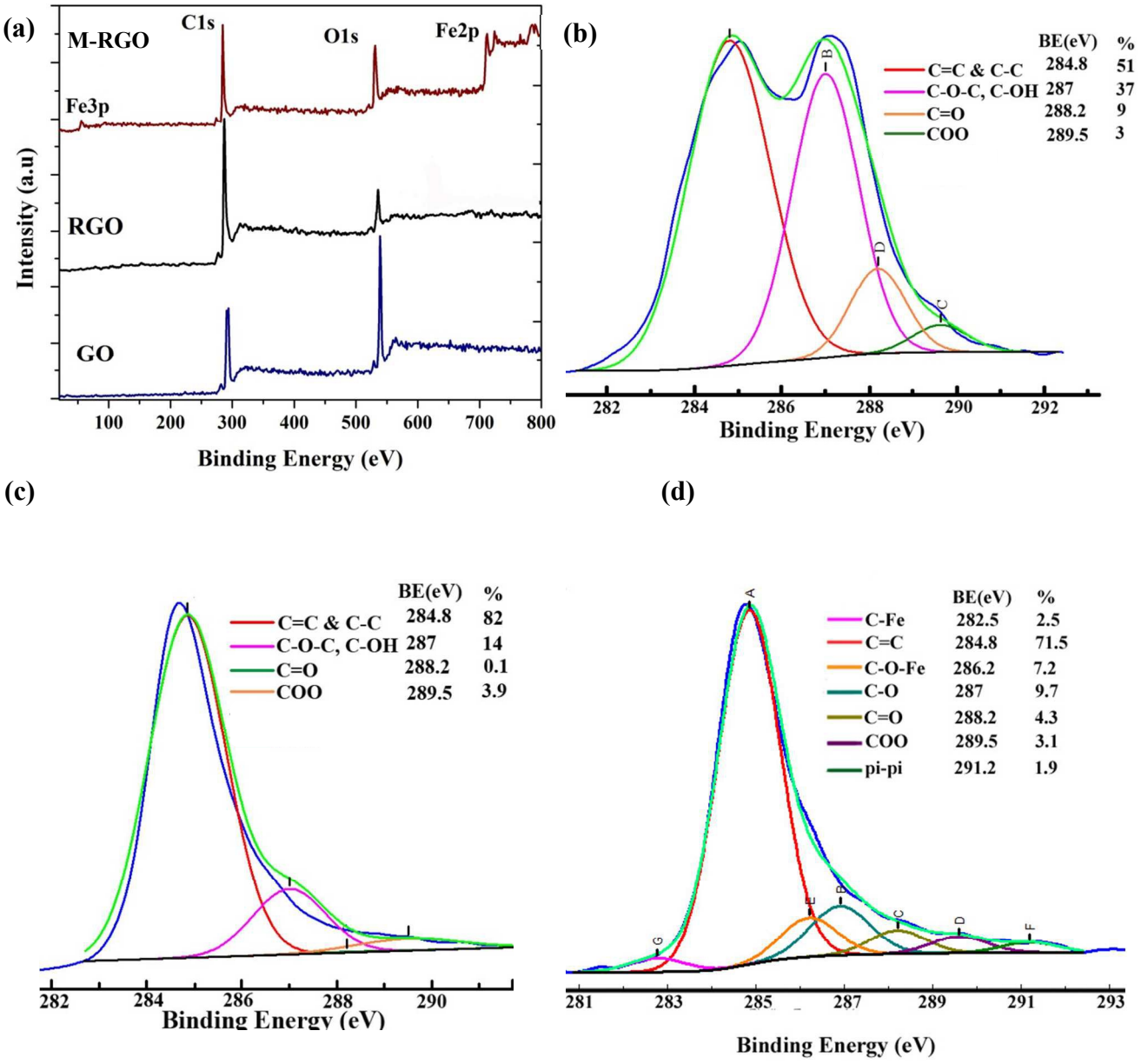

Figure 6: (a) The full scan XPS survey of GO, RGO, and M-RGO, C1s spectra of (b) GO, (c) RGO, and (d) M-RGO.

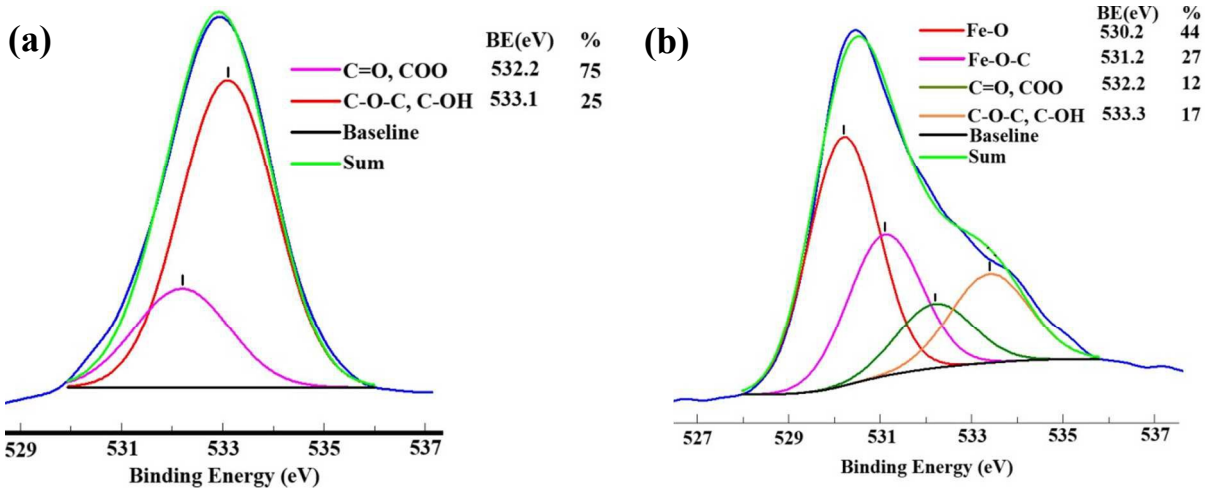

Figure 7: O1s spectra of (a) GO, and (b) M-RGO.

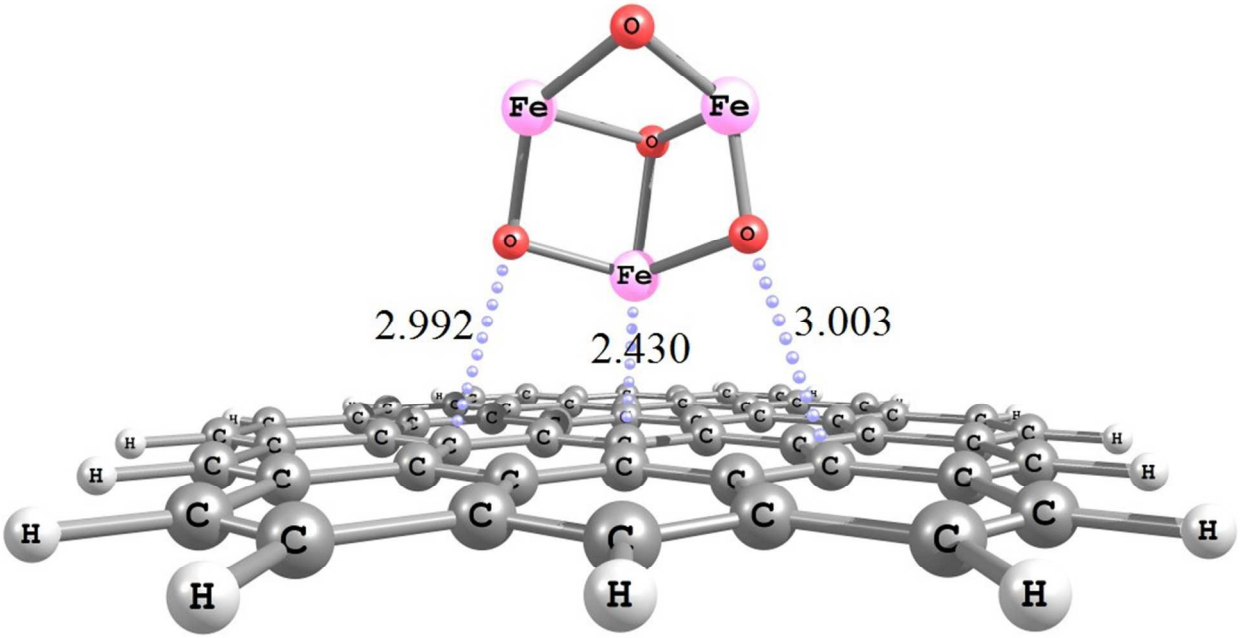

Figure 8: The most stable geometry for adsorption of (Fe_3O_4) cluster on the graphene surface optimized at the M06-2X/cc-pVDZ level of theory.

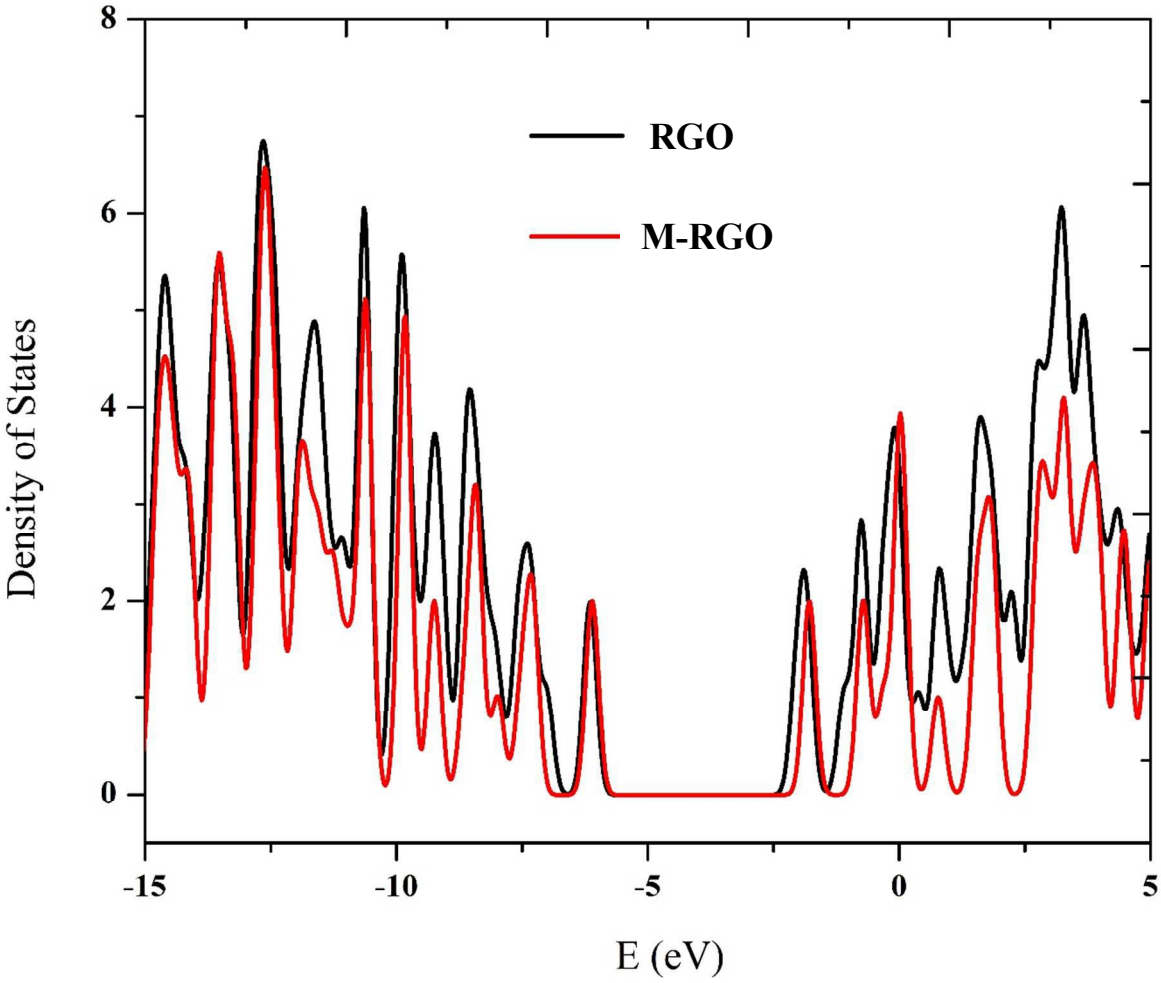

Figure 9: Density of states of RGO compared to M-RGO.

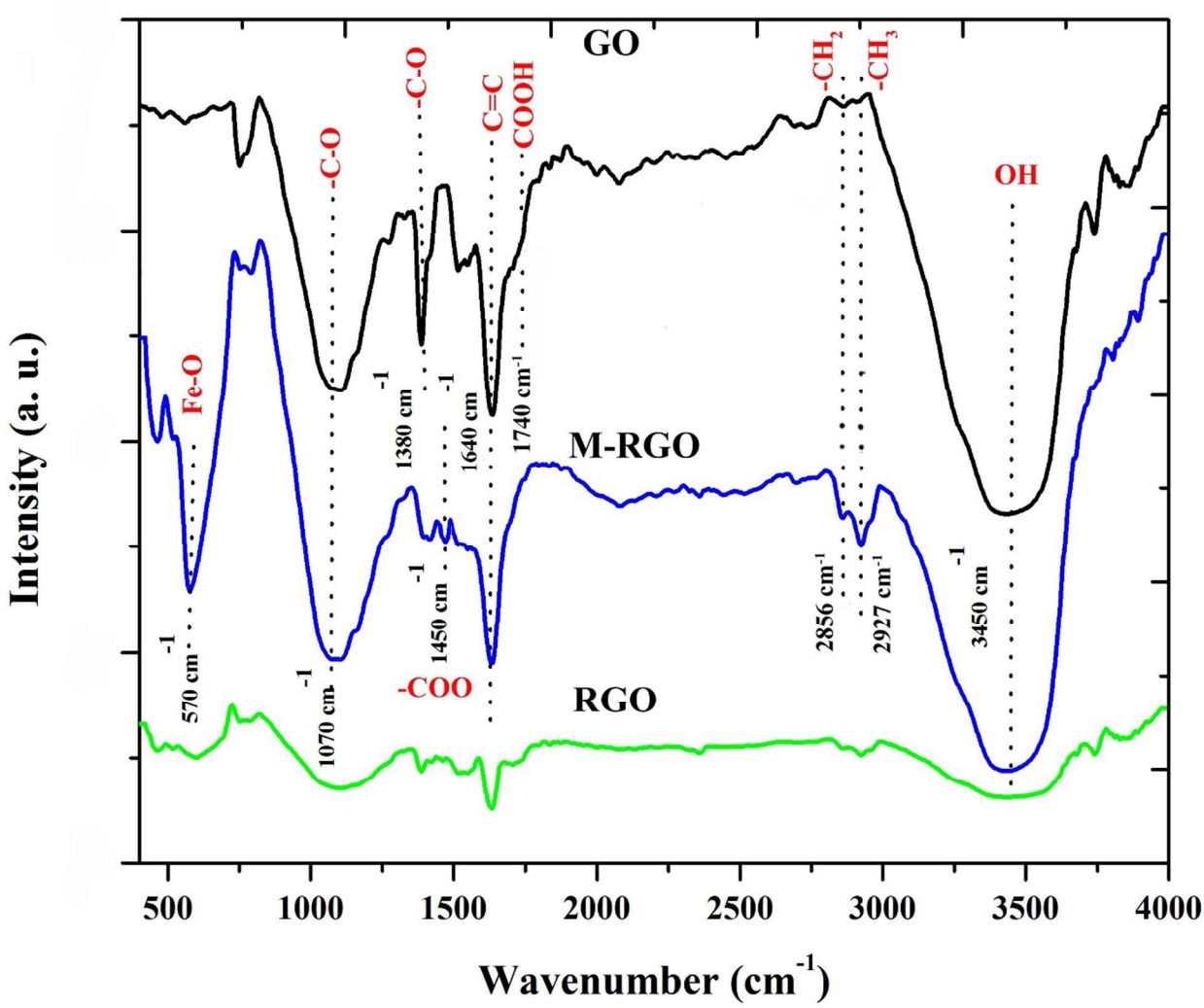

Figure 10: FTIR spectra of GO, RGO, and M-RGO.

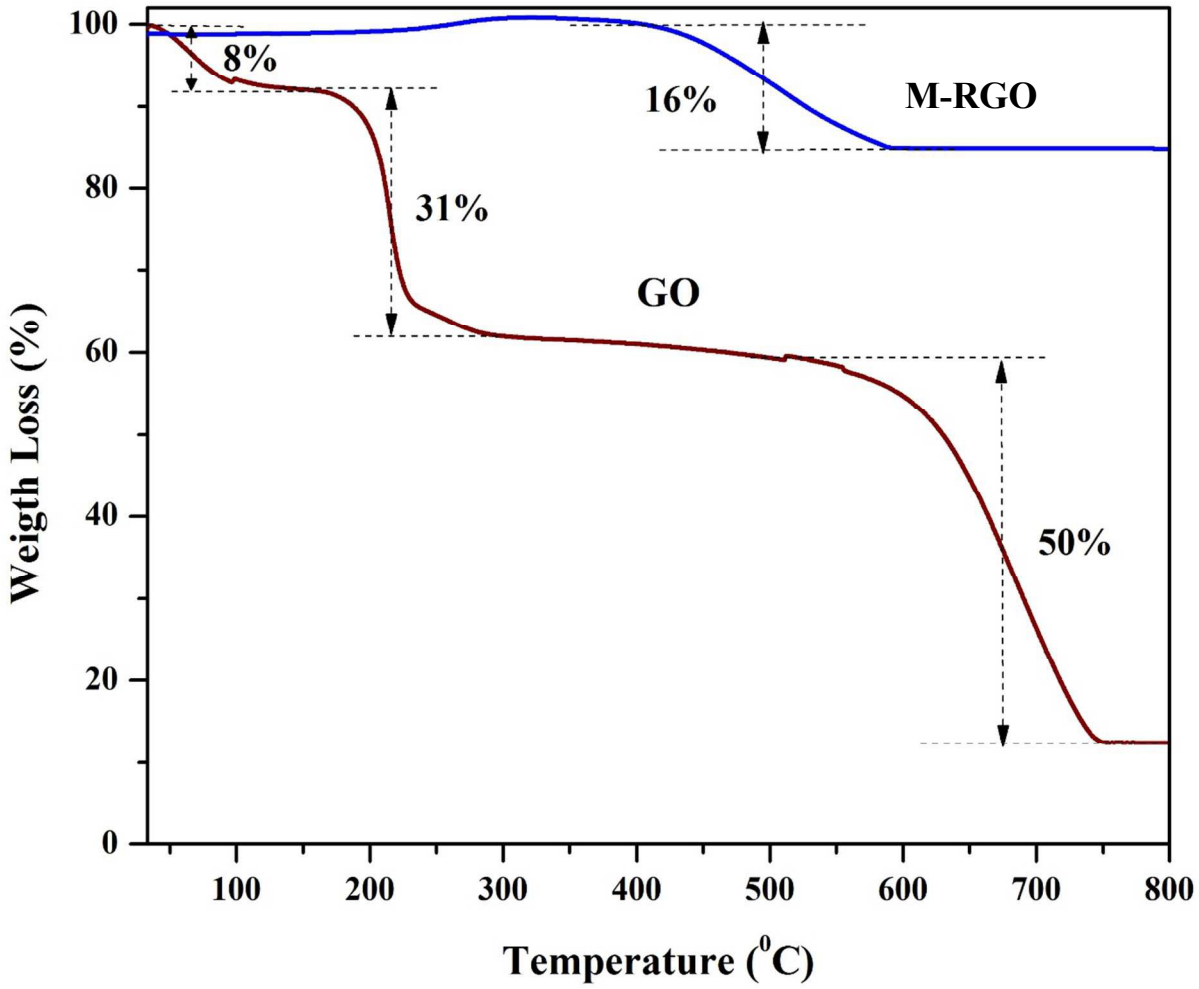

Figure 11: Thermogravimetry analysis (TGA) of GO and M-RGO.

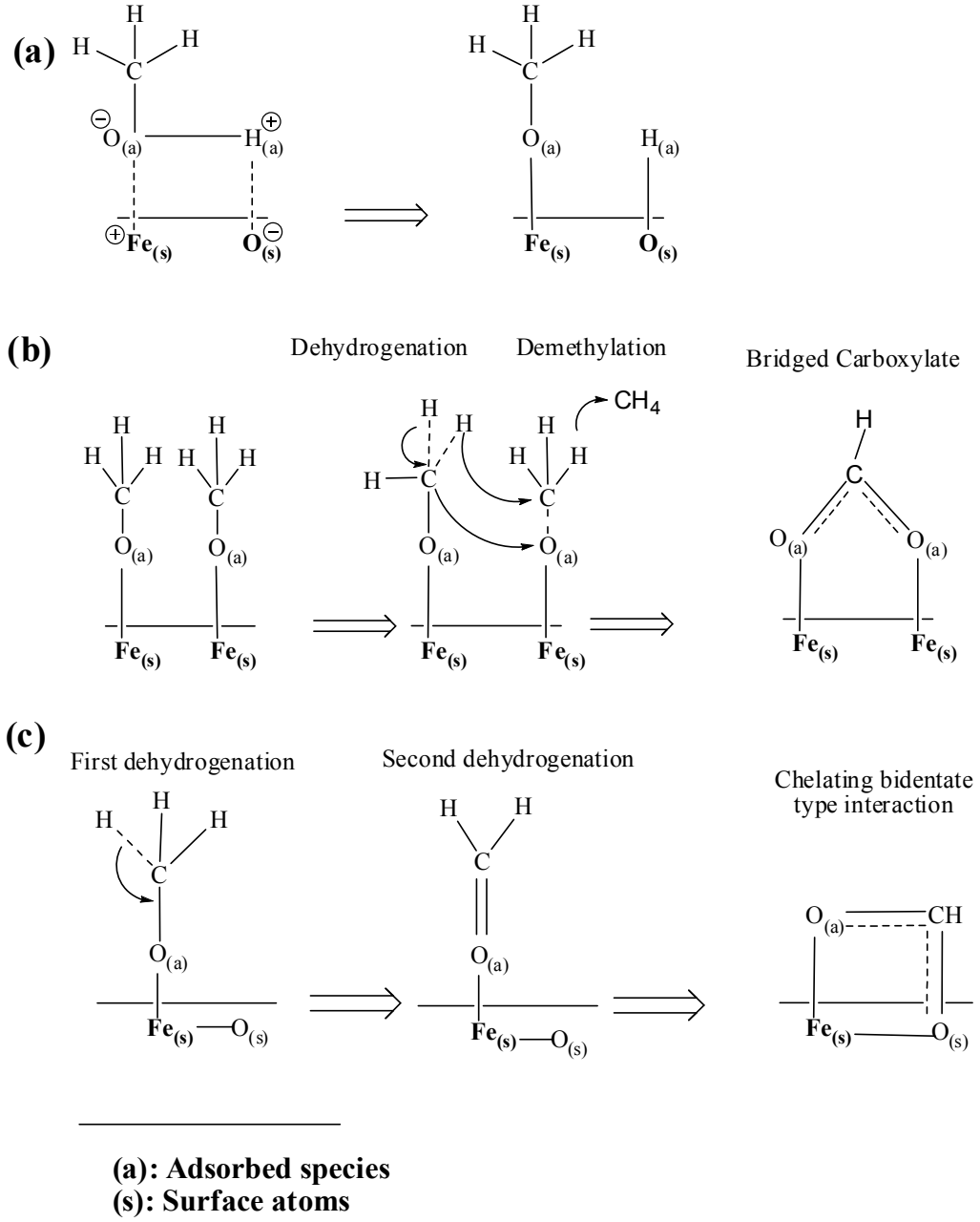

Figure 12: One of the possible pathways for simultaneous interaction of methanol with Fe_3O_4 NPs surface.

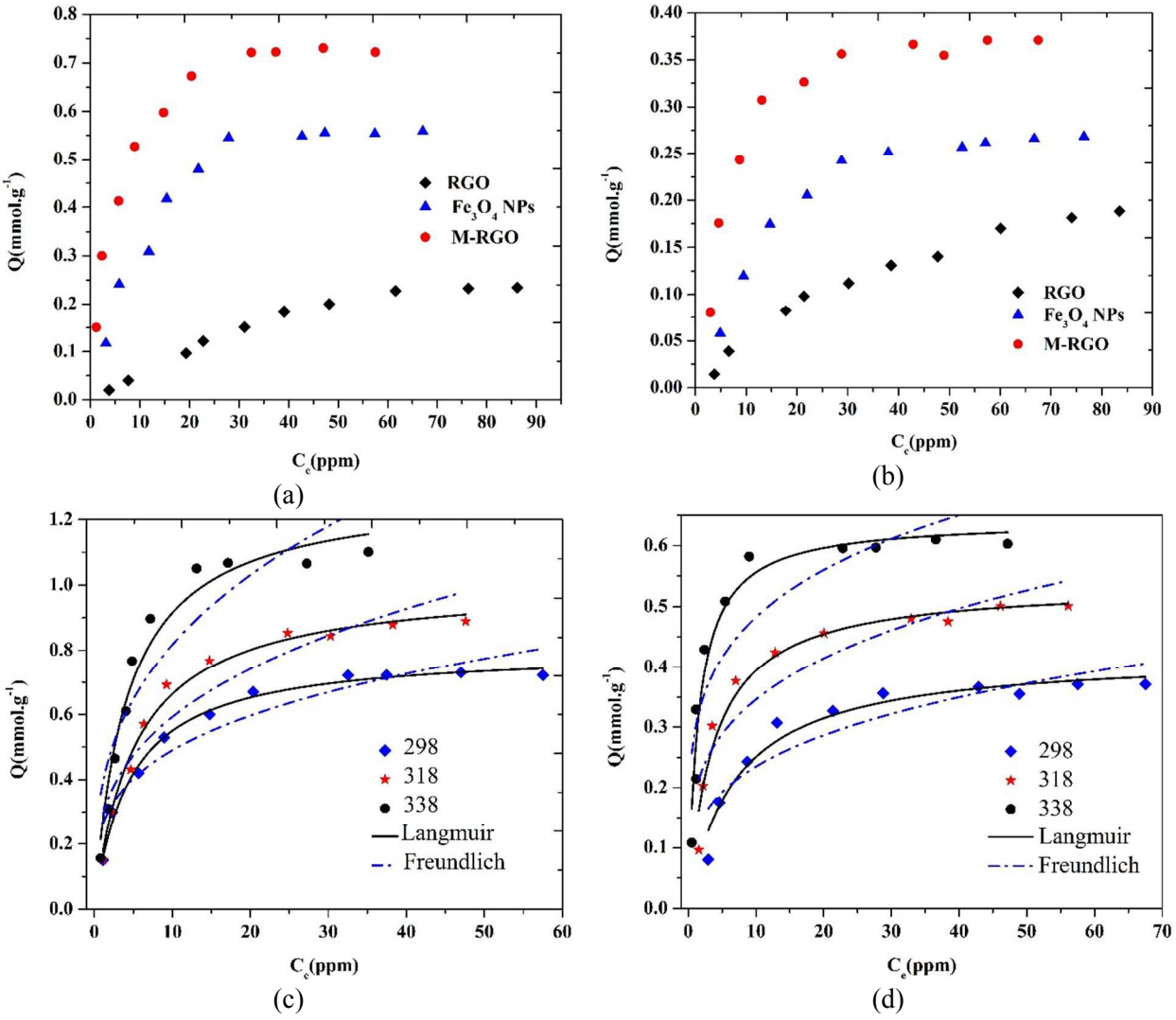

Figure 13: Adsorption isotherms of (a) Co^{2+}, (b) Sr^{2+} ions onto RGO, Fe_3O_4 NPs and M-RGO hybrid, the effect of temperature on adsorption capacity of M-RGO for (c) Co^{2+}, and (d) Sr^{2+} ions.

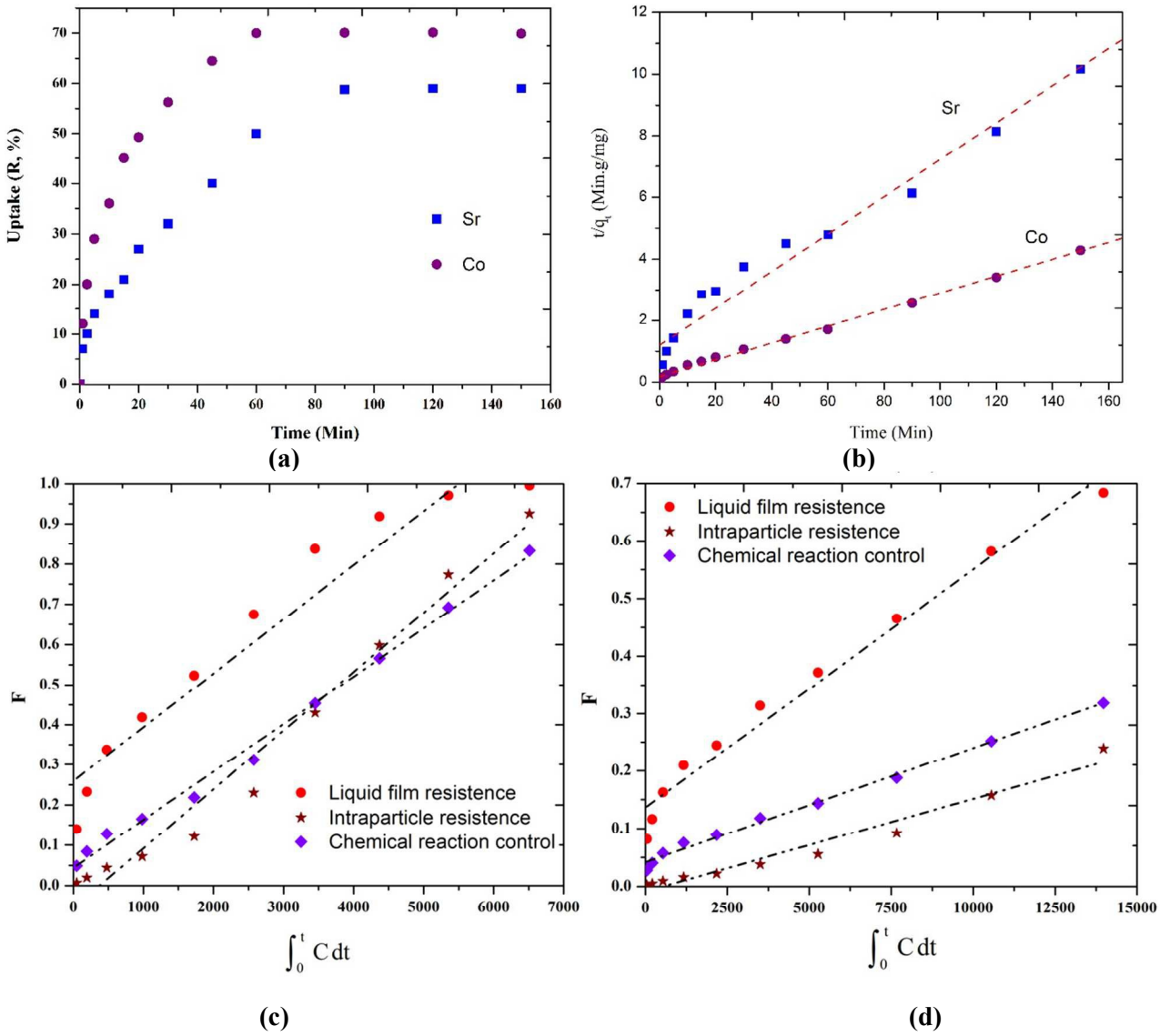

Figure 14: (a) Rate of adsorption of Co^{2+} and Sr^{2+} ions onto M-RGO hybrid, fitting of adsorption data to the (b) pseudo-second order kinetics model, Shrinking core model for (c) Co^{2+} and (d) Sr^{2+} ions in aqueous solution.

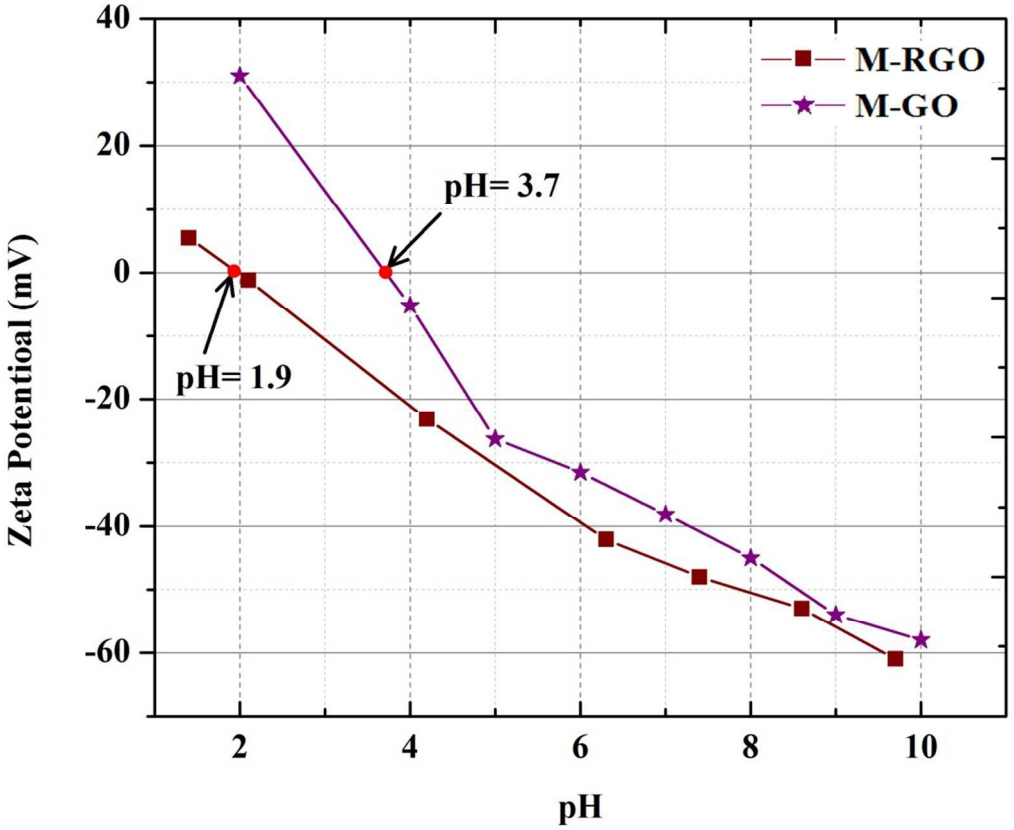

Figure 15: Zeta potential of M-GO and M-RGO versus pH.

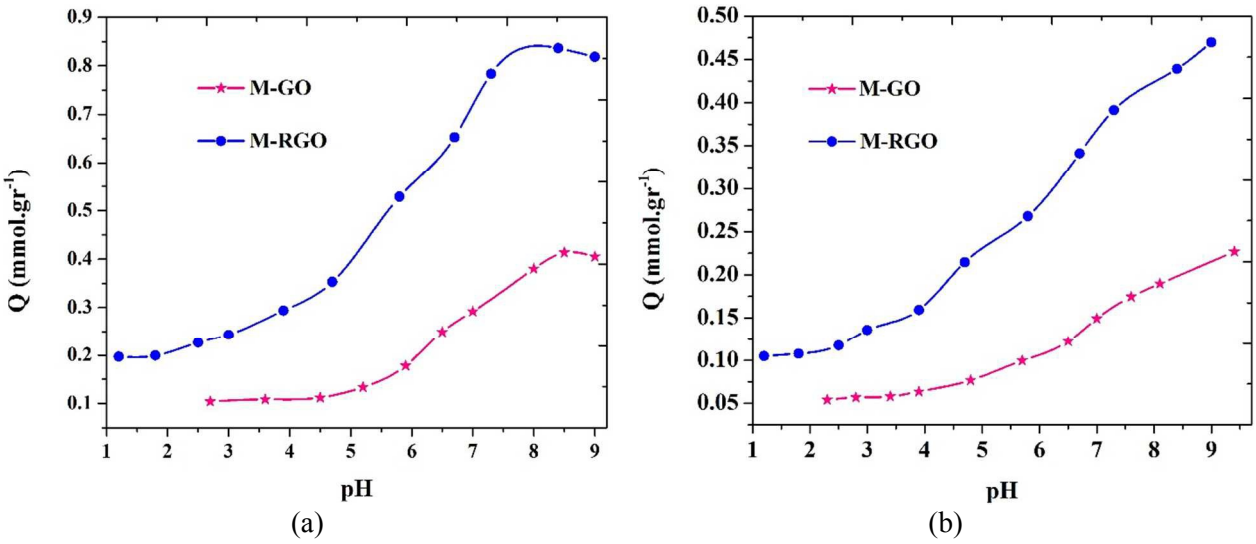

Figure 16: The effect of pH on adsorption of M-GO and M-RGO for (a) Co^{2+}, and (b) Sr^{2+} ions from aqueous solution.

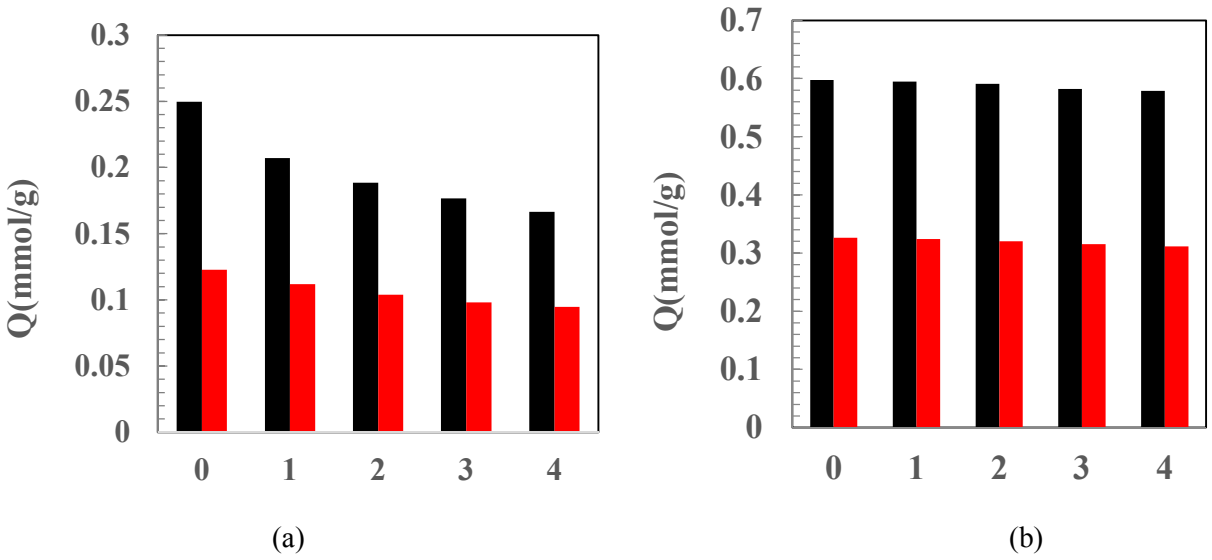

Figure 17: Reusability of Co^{2+} and Sr^{2+} ions onto (a) M-GO, and (b) M-RGO (Black= Co^{2+}, Red=Sr^{2+}).

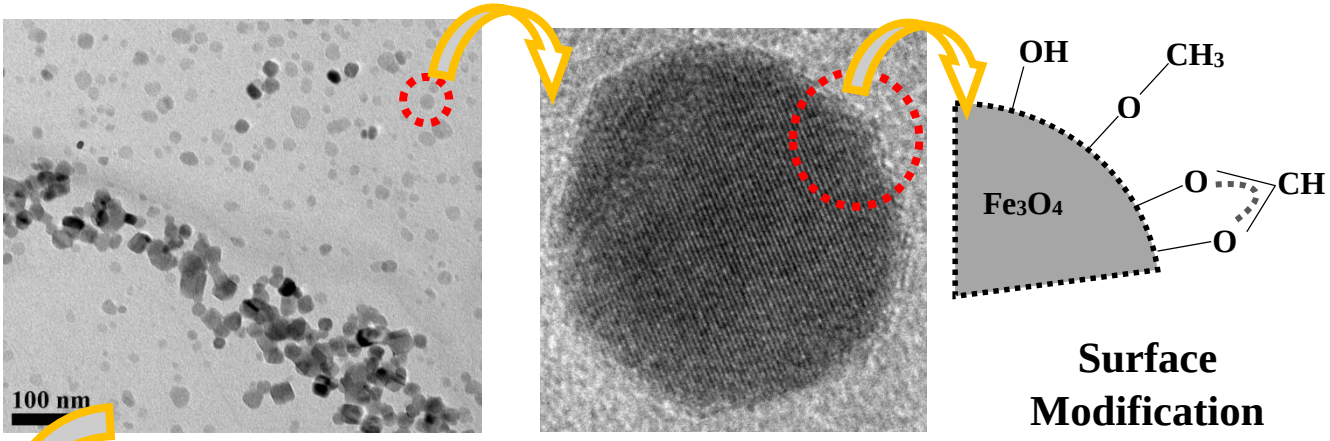

Magnetite-Reduced Graphene Oxide

Magnetite NPs

Surface Modification

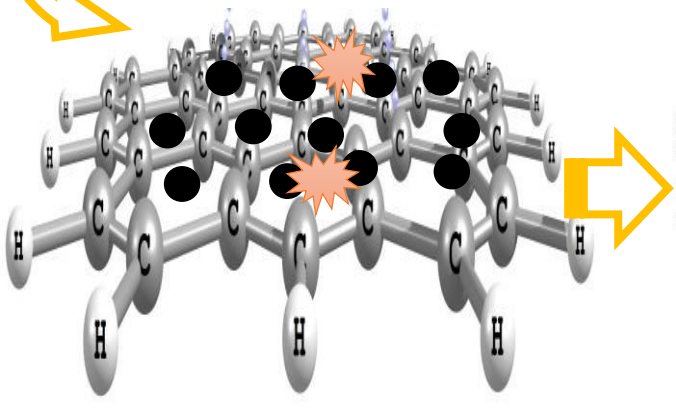

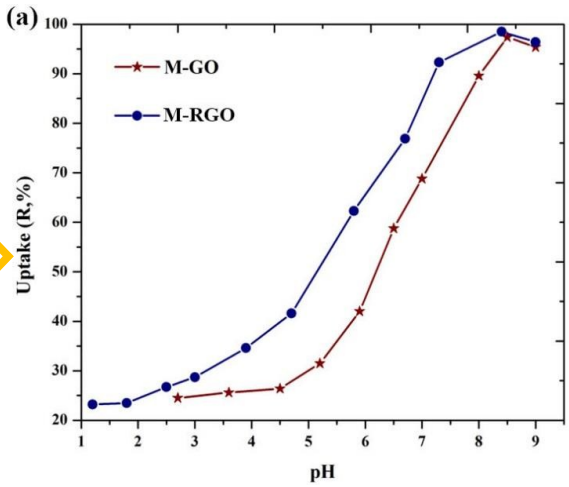

Adsorption of Co^{2+} and Sr^{2+} Onto M-RGO

Enhanced Adsorption Properties of M-RGO

●: Fe3O4 NPs : Co^{2+} or Sr^{2+} ions